



Galaxy interactions in compact groups – II. Abundance and kinematic anomalies in HCG 91c

Frédéric P. A. Vogt,^{1,2*} Michael A. Dopita,^{1,3,4} Sanchayeeta Borthakur,² Lourdes Verdes-Montenegro,⁵ Timothy M. Heckman,² Min S. Yun⁶ and Kenneth C. Chambers⁴

¹Research School of Astronomy and Astrophysics, Australian National University, Canberra, ACT 2611, Australia

²Department of Physics and Astronomy, Johns Hopkins University, 3400 N. Charles Street, Baltimore, MD 21218, USA

³Astronomy Department, King Abdulaziz University, PO Box 80203, Jeddah, Saudi Arabia

⁴Institute for Astronomy, University of Hawaii at Manoa, 2680 Woodlawn Drive, Honolulu, HI 96822, USA

⁵Instituto de Astrofísica de Andalucía, CSIC, Apdo. Correos 3004, E-18080 Granada, Spain

⁶Department of Astronomy, University of Massachusetts, Amherst, MA 01003, USA

Accepted 2015 April 2. Received 2015 March 23; in original form 2014 October 12

ABSTRACT

Galaxies in Hickson Compact Group 91 (HCG 91) were observed with the WiFeS integral field spectrograph as part of our ongoing campaign targeting the ionized gas physics and kinematics inside star-forming members of compact groups. Here, we report the discovery of H II regions with abundance and kinematic offsets in the otherwise unremarkable star-forming spiral HCG 91c. The optical emission line analysis of this galaxy reveals that at least three H II regions harbour an oxygen abundance ~ 0.15 dex lower than expected from their immediate surroundings and from the abundance gradient present in the inner regions of HCG 91c. The same star-forming regions are also associated with a small kinematic offset in the form of a lag of $5\text{--}10 \text{ km s}^{-1}$ with respect to the local circular rotation of the gas. H I observations of HCG 91 from the Very Large Array and broad-band optical images from Pan-STARRS (Panoramic Survey Telescope And Rapid Response System) suggest that HCG 91c is caught early in its interaction with the other members of HCG 91. We discuss different scenarios to explain the origin of the peculiar star-forming regions detected with WiFeS, and show that evidence points towards infalling and collapsing extraplanar gas clouds at the disc–halo interface, possibly as a consequence of long-range gravitational perturbations of HCG 91c from the other group members. As such, HCG 91c provides evidence that some of the perturbations possibly associated with the early phase of galaxy evolution in compact groups impact the star-forming disc locally, and on sub-kpc scales.

Key words: ISM: abundances – H II regions – galaxies: evolution – galaxies: individual: HCG 91c – galaxies: interactions – galaxies: ISM.

1 INTRODUCTION

The environment is known to be a key factor influencing the pathways of galaxy evolution. However, the interconnectivity between the large-scale, environmental mechanisms (e.g. gravitational interactions, ram pressure stripping) and the internal galactic processes (starburst, star formation quenching, nuclear activity and both inflows and outflows) remains poorly understood. Part of the issue lies in the fact that galaxies are spatially extended objects, but are often represented with a series of *ensemble properties* in single-spectrum

studies. The advent of integral field spectroscopy (IFS) has opened a new way to study galaxies and their evolution on a spatially resolved basis at optical and near-IR wavelengths. The wealth of IFS surveys that have been undertaken in recent years provides direct evidence of the scientific potential of spatially resolved studies of a statistically significant number of galaxies. Such surveys include SAURON (Bacon et al. 2001; de Zeeuw et al. 2002; Emsellem et al. 2004), PINGS (Rosales-Ortega et al. 2010), ATLAS^{3D} (Cappellari et al. 2011), CALIFA (Sánchez et al. 2012), SAMI (Croom et al. 2012), VENGA (Blanc et al. 2013), S7 (Dopita et al. 2014, 2015) and MaNGA (Bundy et al. 2014; Drory et al. 2015).

In this paper, we continue our analysis of the ionized gas physics and kinematics associated with star-forming galaxies inside

* E-mail: frederic.vogt@anu.edu.au

compact groups started in Vogt, Dopita & Kewley (2013). Compact groups are isolated structures by definition, and are as such often described as *perfect laboratories* to study the consequences of strong, multiple, simultaneous gravitational interactions on galaxies. Compact groups are intrinsically less crowded than clusters (although they can be denser, see Hickson et al. 1992), so that the detailed structure of their large-scale environment can in principle be better understood. In groups, galaxies are to a first approximation mostly subject to gravitational interactions (Coziol & Plauchu-Frayn 2007), but the role of other processes such as ram pressure stripping remains uncertain.

Indeed, the presence of a hot halo inside some compact groups has been confirmed observationally with a *ROSAT* survey by Ponman et al. (1996). The analysis of *Chandra* observations by Desjardins et al. (2013) showed that in some compact groups (and unlike in clusters), the diffuse X-ray emission is associated with individual galaxy members. Yet, other X-ray bright and massive systems have been found to match the X-ray scaling relations of clusters, and may be representative of an evolved state of compact groups (Desjardins et al. 2014). Galaxies in compact groups are found to be H₁ deficient (when compared to isolated galaxies with similar characteristics). Verdes-Montenegro et al. (2001) reported a correlation between H₁ deficiency and X-ray emission, suggesting galaxy–hot IGM (Intergalactic Medium) interactions as a possible origin for the observed H₁ deficiency. Yet, Rasmussen et al. (2008) report in a *Chandra* and *XMM-Newton* study the non-detection of X-ray emission in four (out of eight) of the most H₁-deficient compact groups of Verdes-Montenegro et al. (2001), suggesting that galaxy–hot IGM interactions (e.g. ram pressure stripping) may in fact not be the mechanism driving the observed H₁ deficiency. The detection of warm H₂ emission at levels inconsistent with X-ray heating or AGN (active galactic nuclei) activity in 32 out of 74 galaxies in 23 compact groups has lead Cluver et al. (2013) to propose that shocks induced by galaxies interacting with a cold IGM may be present in many compact groups. The Stefan’s Quintet compact group and its intergalactic shock represent an extreme example of this mechanism (Appleton et al. 2006; Cluver et al. 2010).

Within the larger scheme of galaxy evolution, it has been suggested that galaxies first start to evolve in compact group-like environments, before further processing in clusters. This is usually referred to as ‘pre-processing’ (Cortese et al. 2006; Vijayaraghavan & Ricker 2013). Pre-processing mechanisms may not be restricted to compact groups and could be active over a wider range of environments (Cybulski et al. 2014), but compact groups in particular favour a more rapid evolution of galaxies compared to the field. The existence of a gap in the mid-infrared colour distribution for galaxies in compact groups compared to the field has been interpreted as the ability of these dense environments to rapidly transform star-forming galaxies into passive ones (Johnson et al. 2007; Gallagher et al. 2008; Walker et al. 2010, 2012). Based on the UV properties of galaxies in groups, Rasmussen et al. (2012) report that at fixed stellar mass, the specific star formation rate (ssSFR) of group members is ~ 40 per cent less than in the field; a trend best detected for galaxies with masses $\lesssim 10^9 M_\odot$. In the case of elliptical galaxies, de la Rosa et al. (2007) found their stellar population to be older by 1.6 Gyr and more metal-poor by 0.11 dex in [Z/H] compared to similar galaxies in the field, which they interpreted as the signature of truncated star formation in these systems. Yet, most galaxies in compact groups appear to follow the *B*-band Tully–Fischer relation (Mendes de Oliveira et al. 2003; Torres-Flores et al. 2010), as well as the *K*-band Tully–Fischer relation (Torres-Flores et al. 2013).

Whether quenched or enhanced, changes in the star formation activity in a galaxy are merely a consequence of the formation, destruction, processing, spatial redistribution and local density variations of the molecular gas (i.e. the fuel) within the system. Therefore, understanding the large-scale gas flows in compact groups is key to a better understanding of the evolutionary pathways of galaxies in these environments. For example, Verdes-Montenegro et al. (2001) proposed an evolutionary sequence for compact groups, where the H₁ gas distribution is first associated with the individual galaxies, before gravitational interactions strip it apart, resulting in no H₁ gas left in the galaxies, or possibly (but less frequently) in a large common envelope.

Here, we describe the use of the WiFeS integral field spectrograph to study the physics and kinematics of the ionized gas in star-forming galaxies inside compact groups. This approach is complementary to group-wide H₁ observations (e.g. Verdes-Montenegro et al. 2001) in that we focus on a different phase of the interstellar medium, and zoom in on the stellar and ionized gaseous content of the galaxies themselves. By targeting galaxies at $z \lesssim 0.03$ with a spectral resolution $R = 7000$ and a spectral pixel (spaxel) size of 1 arcsec² (with natural seeing), we gain access to the physics of the ionized gas on scales of ~ 1 kpc and simultaneously resolve velocity dispersions down to $\sigma \gtrsim 20$ km s⁻¹: an ideal combination to detect and study localized consequences of the compact group environment on galaxies.

Our targets are drawn from both the Hickson and Southern Compact Groups. The Hickson Compact Groups (HCGs, Hickson 1982a,b) represent a class of compact groups that was first identified on Palomar Sky Survey red prints as groups of four or more galaxies with specific brightness, compactness and isolation selection criteria. Most were later on confirmed to be gravitationally bound (Hickson et al. 1992; Ponman et al. 1996). Along with their southern sky cousins (Southern Compact Group or SCG, Iovino 2002), the proximity of these low-redshift systems (median $z \approx 0.03$, Hickson et al. 1992) make them optimum targets for spatially and spectrally detailed observations.

In Vogt et al. (2013), we focused on NGC 838 in HCG 16, confirmed the presence of a large-scale galactic wind and characterized it as young, photoionized and asymmetric, very much unlike the nearby shock-excited galactic wind of NGC 839 (Rich et al. 2010). In this paper, we turn our attention to HCG 91c, a star-forming spiral of which the basic characteristics are given in Table 1. In an effort to tie the large-scale structure of the group to the local environment within the optical disc of HCG 91c, we supplement our optical IFS observations with H₁ observations from the Very Large Array (VLA) and with broad-band optical images from the Pan-STARRS survey. Effectively, we build a multiphase, multiscale view of HCG 91c to understand the presence of abundance and velocity offsets in some of the H_{II} regions detected with WiFeS inside this galaxy.

The paper is structured as follows. We first discuss our different data sets (including their acquisition, reduction and processing) in Section 2. We then describe the group-wide structure and kinematic of the H₁ gas in HCG 91 in Section 3, and zoom-in on HCG 91c in Section 4. We discuss possible connections between group-wide mechanisms and specific star-forming regions inside HCG 91c in Section 5, and summarize our conclusions in Section 6.

Throughout this paper and unless noted otherwise, when we refer to specific emission lines we mean $[N\,\text{II}] \equiv [N\,\text{II}]\lambda 6583$, $[S\,\text{II}] \equiv [S\,\text{II}]\lambda 6717 + \lambda 6731$, $[O\,\text{II}] \equiv [O\,\text{II}]\lambda 3727 + \lambda 3729$ and $[O\,\text{III}] \equiv [O\,\text{III}]\lambda 5007$. We adopt the maximum likelihood cosmology from Komatsu et al. (2011): $H_0 = 70.4$ km s⁻¹ Mpc⁻¹, $\Omega_\Lambda = 0.73$ and $\Omega_M = 0.27$, resulting in a distance to HCG 91c of 104 Mpc.

Table 1. Basic characteristics of HCG 91c.

Property	Value	Ref.
Names	HCG 91c ESO 467 – G 013	
R.A. (J2000)	22 ^h 09 ^m 07 ^s	
Dec. (J2000)	-27°48'34"	
Redshift	0.024 414 0.024 377	(a) (b)
Radial velocity	7319 km s ⁻¹ 7308 km s ⁻¹	(a) (b)
Distance	104 Mpc	
Spatial scale	504 pc arcsec ⁻¹	
Diameter	50 arcsec ≈ 25 kpc	(b)
R_{25}	26.75 ± 3.25 arcsec	(c)
Absolute rotation velocity (at radii > 22 kpc)	100 ± 11 km s ⁻¹	(b)
Star formation rate	2.19 M _⊙ yr ⁻¹ 2.10 ± 0.06 M _⊙ yr ⁻¹	(d) (b)
Stellar mass	$1.86 \times 10^{10} M_{\odot}$	(d)
H _i mass	$2.3 \times 10^{10} M_{\odot}$	(e)

References: (a) Hickson et al. (1992), (b) this work, (c) de Vaucouleurs et al. (1991), (d) Bitsakis et al. (2014), (e) Borthakur, Yun & Verdes-Montenegro (2010).

2 OBSERVATIONAL DATA SETS

2.1 WiFeS

2.1.1 Observations

We observed HCG 91c with WiFeS, the Wide-Field Integral Field Spectrograph (Dopita et al. 2007, 2010) mounted on the 2.3 m telescope (Mathewson et al. 2013) of the Australian National University at Siding Spring Observatory in Northern New South Wales, Australia. The footprint of our observation is shown in Fig. 1, overlaid on a red band image from the Second Digitized Sky Survey

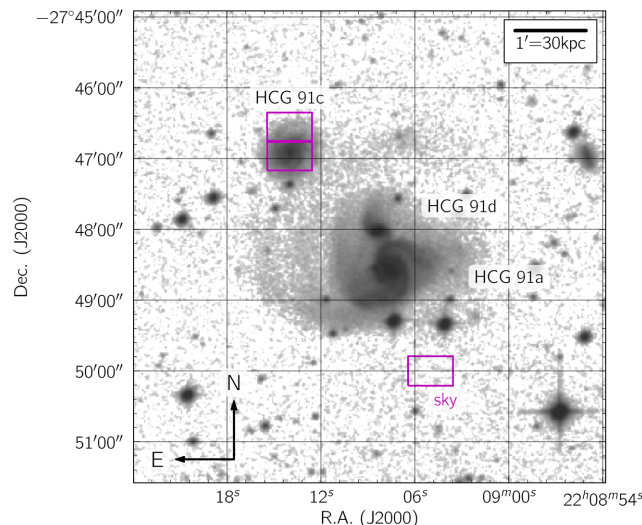


Figure 1. Red band image of HCG 91a, c and d from DSS-2. The purple rectangles denote the footprint of our WiFeS observations of HCG 91c. The location of the sky field was chosen to avoid any of the faint and extended tidal structures stemming from HCG 91a, including the faint tidal arm extending (on-sky) from HCG 91a to HCG 91c.

(DSS-2).¹ We combined two individual WiFeS pointings to construct a 38×50 arcsec² mosaic in order to better cover the spatial extent of HCG 91c.

The data was acquired over two nights on 2012 August 15 and 16, with a seeing of 1.2–1.5 arcsec. Each individual science field of 25×38 arcsec² was observed 4×1400 s, resulting in 5600 s on-source per field. A blank patch of sky to the south-west of HCG 91a was observed for a total integration time of 700 s between every pair of consecutive science frames.

WiFeS is a dual-beam integral field spectrograph with independent red and blue channels. We used the B3000 grating for the blue arm and the R7000 grating for the red arm, in conjunction with the RT560 dichroic. This set-up allows us to have a complete wavelength coverage from 3800 to 7000 Å, as well as a high spectral resolution observation of the H α emission line to perform a detailed kinematic analysis. It is important to note here that with this instrumental setting, the final spectra associated with each spaxel in the mosaic has a dual spectral resolution of $R = 3000$ from 3800 to 5560 Å and $R = 7000$ from 5560 to 7000 Å, corresponding to a full width at half-maximum for emission lines of ~ 100 and ~ 43 km s⁻¹, respectively.

2.1.2 Data reduction

Each science exposure was individually bias subtracted, flat fielded, sky subtracted, wavelength and flux calibrated, as well as atmospheric refraction corrected with PYWIFES (v0.5.6), the new official PYTHON data reduction pipeline for WiFeS observations (Childress et al. 2014a,b). This new pipeline entirely replaces the now obsolete IRAF² pipeline (Dopita et al. 2010) by providing several key improvements: scriptability, reproducibility, advanced wavelength calibration technique using an accurate model of the instrument's optics, multicore processing and compatibility with the first and second generations of CCD detectors in the WiFeS cameras. The pipeline is described in detail in Childress et al. (2014b), to which we refer the reader for more details about the different functions.

The reduced eight red science frames and eight blue science frames are median combined in two mosaics (red and blue) using a custom made PYTHON script. Because the wavelength sampling was chosen to be the same during the data reduction process, mosaicking only requires a shift of the data cubes in the spatial x and y directions. Given the seeing conditions and the WiFeS spaxel size of 1×1 arcsec², we restrict ourselves to integer spatial shifts. The final mosaic contains $38 \times 50 = 1900$ spaxels. Once the red and blue mosaics are constructed, we correct them for Galactic extinction using the Schlafly & Finkbeiner (2011) recalibration of the Schlegel, Finkbeiner & Davis (1998) extinction map based on dust emission measured by COBE/DIRBE and IRAS/ISSA. We assume for HCG 91c a Galactic extinction $A_V = 0.052$, following the NASA/IPAC Extragalactic Database (NED). The recalibration assumes a Fitzpatrick (1999) reddening law with $R_V = 3.1$ and a different source spectrum than that used by Schlegel et al. (1998).

We note that the far blue end of a WiFeS spectrum below 4000 Å (with the B3000 grating) is a known problematic region. The core

¹ The DSS-2 data were obtained from the European Southern Observatory Online Digitized Sky Survey Server.

² IRAF is distributed by the National Optical Astronomy Observatories, which are operated by the Association of Universities for Research in Astronomy, Inc., under cooperative agreement with the National Science Foundation. See <http://iraf.noao.edu>.

reason, aside of a drop of the overall instrument transmission, is that the available flat-field lamps (at the epoch of our observations) have almost no flux at these wavelengths. It is therefore virtually impossible to accurately flat-field the data below 4000 Å with the B3000 grating. PYWIFES combines lamp flat-field images with twilight sky flat-field images which mitigate this issue partially, but not entirely. In the present case, this flat-fielding issue directly affects the [O II] flux, to which we find a correction factor of 1.5 ought to be applied. This correction factor is only an average for the entire field of view, so that we decided not to rely on the [O II] line flux in our spaxel-based analysis of HCG 91c.

2.1.3 Spectral fitting

We fit the strong emission lines for all 1900 spaxels in our mosaic after fitting and removing the underlying stellar continuum in the spectra. This task is performed automatically using the custom build LZIFU v0.3.1 IDL routine, written by I-Ting Ho at the University of Hawaii (Ho et al. 2014, Ho et al., in preparation). LZIFU is a modified version of the UHSPECFIT IDL routine to which D. S. N. Rupke, J. A. Rich and H. J. Zahid all contributed. The code is a wrapper around PPXF (Cappellari & Emsellem 2004), used to perform the continuum fitting, and MPFIT (Markwardt 2009), used to fit the emission lines with different Gaussian components.

The LZIFU routine first performs (via PPXF) the continuum fitting by looking at spectral regions free of emission lines. We refer the reader to the PPXF documentation for further details. We use the González Delgado et al. (2005) set of stellar templates with the Geneva isochrones to construct the best-matched stellar continuum for each spaxel. We note that we tested using the stellar templates based on the Padova isochrones instead, but found no significant difference in the fit results.

LZIFU offers the possibility to fit one or multiple Gaussian components to multiple emission lines simultaneously. In the present case, a visual inspection of the data revealed a very narrow structure of the different emission lines with no evidence of multiple peaks in any spaxel. For consistency, we performed two distinct fits of the emission lines – with one, and subsequently with two Gaussian components. We detected the presence of a broadened base around the H α emission line in the \sim 100 brightest spaxels, and confirmed the detection with a statistical f-test (e.g. Westmoquette et al. 2007). We performed this test blindly for the [N II] and H α emission lines only for all spaxels, and with a null-hypothesis rejection probability of 0.01. However, because (a) the broadened base is visually only marginally detected around the H α line in \sim 10 out of 1081 spaxels with signal-to-noise (S/N) larger than 5, (b) it is not detected around any other emission line, and (c) beam-smearing effects may be responsible for some of the broad component, we choose to enforce a one-Gaussian component fit for every spaxel in our mosaic of HCG 91c.

We note here that nowhere in our observations do we detect clear multiple peaks in the emission line profile of H α as reported by Amram et al. (2003) in their Fabry–Perot observations of HCG 91c. Although the spectral sampling (0.35 Å) and spectral resolution ($R = 9375$ at H α) of their data are slightly better than ours (0.44 Å and $R = 7000$), WiFeS (of which the instrumental design minimizes scattered light and other instrumental artefacts) should have clearly detected the distinct velocity components offset by \sim 100 km s $^{-1}$ observed by Amram et al. (2003). A detailed comparison of the WiFeS line profile with the velocity structures of Amram et al. (2003) is presented in Appendix A. With no evidence for multiple

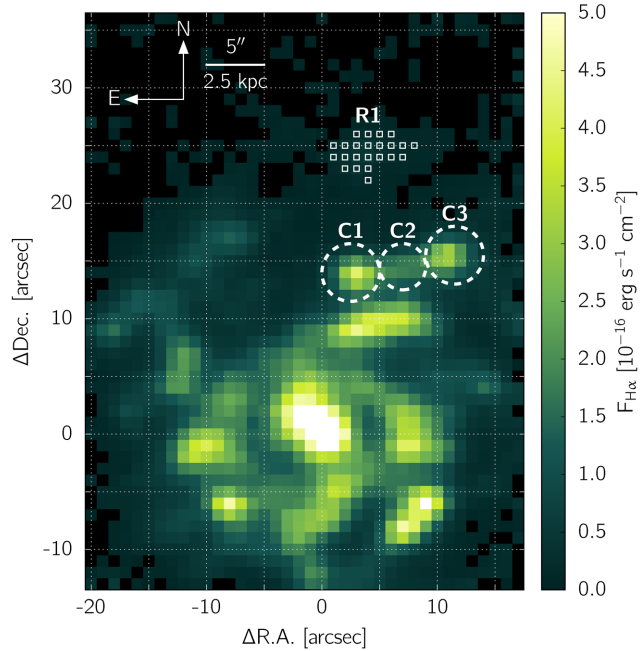


Figure 2. H α flux map of HCG 91c, before correcting the extragalactic reddening. The core of the galaxy and the spiral structure is traced by enhanced H α emission. Three star-forming regions of interest ‘C1’, ‘C2’ and ‘C3’ are labelled accordingly. The region ‘R1’ is also indicated, along with the individual spaxels it comprises. The x- and y-axis are in arcsec (\equiv spaxels), centred on the brightest spaxel in H α . At the distance of HCG 91c, 1 arcsec \approx 503 pc.

components and/or significant asymmetries in the line profiles in our WiFeS observations, we are led to conclude that the gas in HCG 91c is associated to a single kinematic structure at all locations.

The H α flux map of HCG 91c observed by WiFeS is shown in Fig. 2 in units of 10^{-16} erg s $^{-1}$ cm $^{-2}$. The final emission line widths quoted in this paper are corrected for the instrumental resolution.

Throughout this paper, we analyse our WiFeS data set on a *per-spaxel* basis to keep a high spatial resolution even at large distances from the galaxy centre. To ensure trustworthy results, we adopt varying S/N cuts throughout our analysis. For example, we require $S/N(H\alpha;H\beta) \geq 5$ to perform the extragalactic reddening correction. The specific S/N cuts will be discussed individually for each case in the next sections. For clarity, we also include the associated S/N cut and number of spaxel in all relevant diagrams throughout this paper.

A series of spaxels with $S/N(H\alpha) \geq 5$ and $S/N(H\beta) < 5$ are detected to the north of HCG 91c at the mean position [4;25]. This is the most distant star-forming region (from the galaxy centre) detected with WiFeS, and as such it holds unique clues regarding the state of the ionized gas at large radii. To ensure a reliable extragalactic correction, we have summed all of the contiguous spaxels with $S/N(H\alpha) \geq 5$ into a combined spectrum, which we refer to as the ‘R1’ region. The individual R1 spaxels are marked with empty white squares in Fig. 2. We also indicate the location of three star-forming regions with anomalous abundance and kinematics offsets, the ‘C1’, ‘C2’ and ‘C3’ regions.

2.1.4 Extragalactic reddening

We correct our WiFeS observations for extragalactic reddening using the H α /H β line ratio. HCG 91c does not contain any AGN

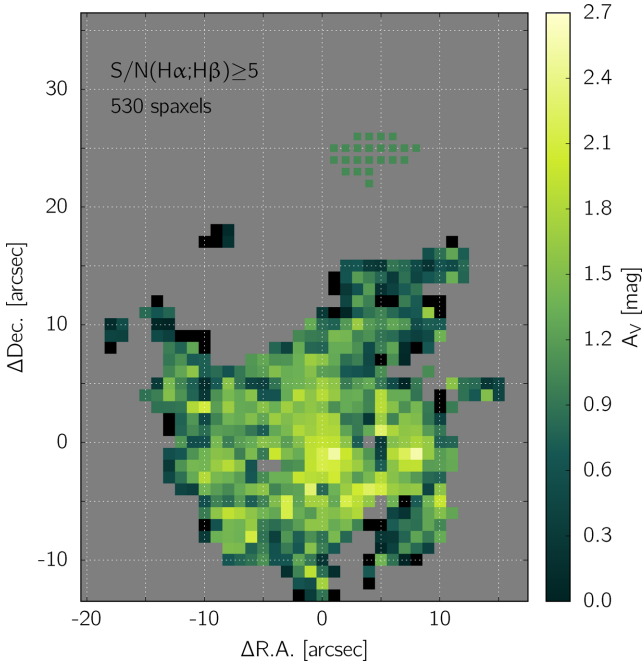


Figure 3. A_V extinction, calculated from the $H\alpha/H\beta$ emission line flux ratio. The centre of the galaxy is the most affected by extragalactic reddening, with $A_V > 2$. Enhanced extinction regions are also associated with the spiral structure detected in Fig. 2. The uncertainty in the A_V value is of the order of 0.6–0.8 for all spaxels.

which could increase the intrinsic line ratio value $R_{\alpha\beta}$, and we therefore assume that $R_{\alpha\beta} = 2.86$ as in a case B recombination ($n_e = 100 \text{ cm}^{-3}$; $T = 10^4 \text{ K}$, see Osterbrock 1989). We follow the methodology described in detail in the appendix of Vogt et al. (2013), and use the extinction curve from Fischera & Dopita (2005) with $R_V^A = 4.5$. The choice of this extinction curve, very similar to that of Calzetti et al. (2000), is motivated by the fact that Wijesinghe et al. (2011) showed that for galaxies in the GAMA survey (Driver et al. 2009), it provides self-consistent estimates of the SFRs computed from the UV, $H\alpha$ and [O III]. The resulting V -band extinction A_V in magnitudes is shown in Fig. 3. The extragalactic reddening (and correction) is only calculated (and applied) for the 530 spaxels with $S/N(H\alpha;H\beta) \geq 5$, corresponding to a line intensity detection threshold of $\sim 2 \times 10^{-17} \text{ erg s}^{-1} \text{ cm}^{-2} \text{ Å}^{-1}$.

The largest extinction is present towards the core of the galaxy with $A_V > 2$. Further out, the extinction drops to $A_V \approx 1$, with localized increases coherent with the spiral arms visible in Fig. 2. Unlike most star-forming regions in the spiral arms, we detect no enhancement of the extinction associated with the C1, C2 and C3 regions at the 1σ level (given an uncertainty of 0.6–0.8 in the A_V value).

2.2 VLA

The H_1 distribution in HCG 91 was observed with the Very Large Array (VLA) under the program AV0285 (P.I. L. Verdes-Montenegro) on 2005 October 5. The observations were carried-out in the VLA D-configuration with 3.25 hr of on-source integration and dual polarization using two intermediate frequencies. The resulting total bandwidth of the data cube is 6.2 MHz ($\sim 1200 \text{ km s}^{-1}$) with a resolution of 97 kHz. The correlator was set up to cover the entire H_1 spectral linewidth with a velocity resolution of $\sim 21.6 \text{ km s}^{-1}$.

The data was calibrated following the standard VLA calibration and imaging procedures using NRAO’s Astronomical Image Processing Software (AIPS). The final absolute uncertainty in the flux density scaling is ~ 10 per cent. The synthesized beam of the reduced data cube is $74 \text{ arcsec} \times 47 \text{ arcsec}$, with a position angle (PA) of $4^\circ 83$ west-of-north (Borthakur et al. 2010).

2.3 Pan-STARRS

HCG 91c was observed at multiple epochs with the Pan-STARRS³ 1 (PS1) telescope (Kaiser et al. 2002, 2010; Kaiser 2004; Hodapp et al. 2004) on Haleakala (Maui) as part of the PS1 3π survey (Chambers et al., in preparation). This survey mapped (several times) the entire sky visible from Hawaii ($\delta > -30^\circ$) in five broad filters ($g_{\text{P1}}: \sim 400\text{--}550 \text{ nm}$; $r_{\text{P1}}: \sim 550\text{--}700 \text{ nm}$; $i_{\text{P1}}: \sim 690\text{--}820 \text{ nm}$; $z_{\text{P1}}: \sim 820\text{--}920 \text{ nm}$; $y_{\text{P1}}: \sim 920\text{--}1000 \text{ nm}$; see Tonry et al. 2012) between 2010 and 2014. The Pan-STARRS images presented in Section 4.1 were obtained from the online Postage Stamp server. These images were automatically processed by the PS1 Image processing Pipeline (see e.g. Magnier 2007; Magnier et al. 2013). Specifically, the Pan-STARRS images presented in this paper (see Fig. 7) have been obtained from the 3π survey processing version 2 release. They have a pixel size of 0.25 arcsec, and are the result of the combination of 20 single epoch exposures obtained under natural seeing conditions (~ 1 arcsec).

3 THE GROUP-WIDE H_1 DISTRIBUTION IN HCG 91

H_1 is an excellent tracer of past and ongoing gravitational interactions. For compact groups, H_1 can also be used to estimate the evolutionary stage of the group overall (Verdes-Montenegro et al. 2001). The H_1 map for HCG 91 obtained with the VLA is shown in Fig. 4. The left-hand and right-hand panels show position–position and position–velocity (PV) projections of the data cube, respectively. Isointensity surfaces are fitted to the distribution of H_1 emission in the three-dimensional data cube using the MAYAVI module in PYTHON (Ramachandran & Varoquaux 2011), before being projected on to the respective two-dimensional planes. Each isointensity level is shown with an 80 per cent transparency, with exception to the innermost one with 0 per cent transparency. The locations of the HCG 91a, b, c and d galaxies are marked with black crosses. The location of the C1, C2 and C3 star-forming regions in HCG 91c is indicated with small golden cubes and black crosses. H_1 structures of interest (see below) are marked with red crosses for rapid identification. A large H_1 tail associated with HCG 91a is traced with a red rod. Fig. 4 is also interactive, following a concept described by Barnes & Fluke (2008). By clicking on it in Adobe ACROBAT READER v9.0 or above, it is possible to load an interactive view of the $(X;Y;v)$ data cube. The interactive model is also accessible via a supplementary HTML file compatible with most mainstream web browsers.⁴ When inspecting this interactive 3D map, one should remember that it is not ‘fully’ spatial, but rather an $X\text{--}Y\text{--}v$ volume. Presenting the VLA 3D data cube as 3D model is similar to the example provided by Kent (2013), although our respective 3D model creation methods are different (i.e. we do not use BLENDER). The total

³ Panoramic Survey Telescope And Rapid Response System.

⁴ At the date of publication, the interactive HTML document is compatible with FIREFOX, CHROME, SAFARI and INTERNET EXPLORER. We refer the reader to the X3DOM documentation for an up-to-date compatibility list: <http://www.x3dom.org/>.

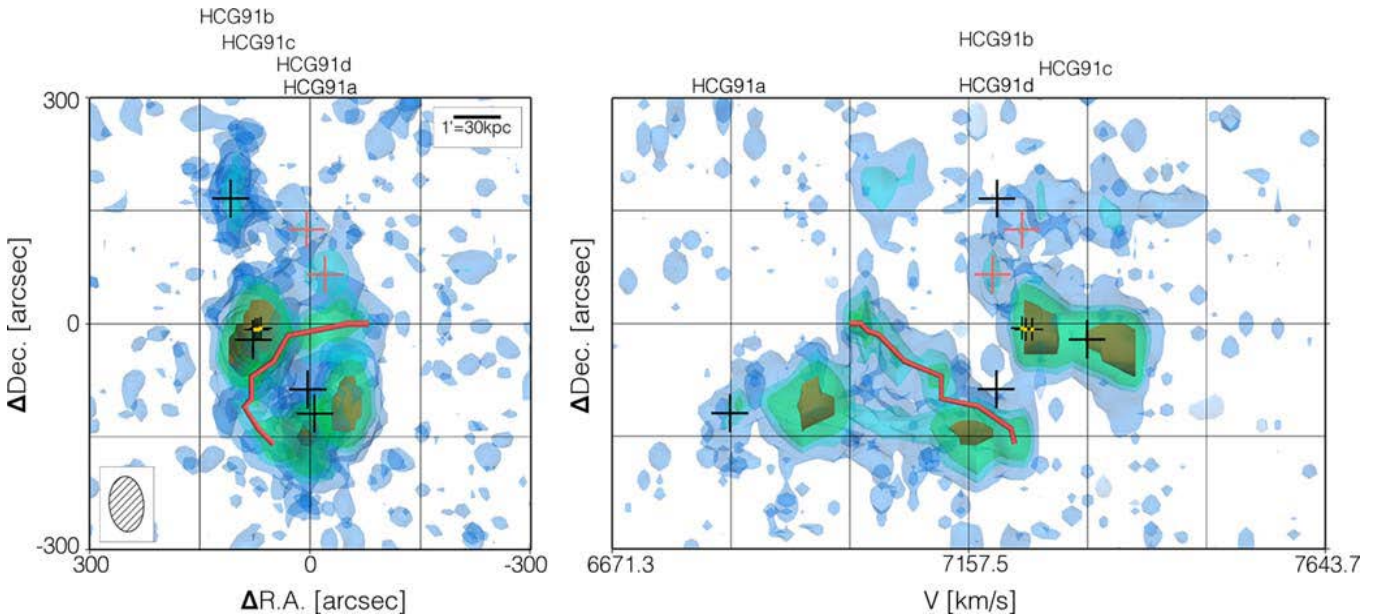


Figure 4. Position–position (left) and PV (right) projection of the H I gas content of HCG 91, as seen by the VLA. The gas density is traced by a series of iso-intensity semitransparent surfaces (set at 1.3, 2.5, 3.5 and 6.0 mJy beam $^{-1}$, respectively). The location of the different group members is marked with black crosses, and labelled accordingly above either panels. Two H I clumps associated with the main gas reserve around HCG 91c are marked with red crosses for unambiguous identification. The large tidal tail originating to the south-east of HCG 91a is traced by a red rod. The C1, C2 and C3 star-forming regions in HCG 91c are marked with golden cubes and black crosses (the golden cubes are 5 arcsec \times 5 arcsec \times 5 km s $^{-1}$ in size). The corresponding VLA beam size (74 arcsec \times 47 arcsec; see Borthakur et al. 2010) is shown to the bottom left of the left-hand panel. An interactive version of this figure can be accessed either with Adobe ACROBAT READER v.9.0 or above by clicking on this figure, or via most mainstream web browsers by opening the corresponding HTML file included as supplementary material to this paper. The 3D cube can be freely rotated and/or zoomed in and out. In the interactive cube, the blue axis is the velocity dimension, the red axis is the R.A. direction, and the green axis the Dec. direction. A series of pre-set views allow the viewer to easily reproduce projections of interest or remove the lowest intensity isosurface for a clearer view of each galaxy. The golden cubes marking the location and spatial/kinematic extent of the C1, C2 and C3 star-forming regions are best seen in the interactive counterpart of this figure.

H I mass associated with HCG 91 is $2.3 \times 10^{10} M_{\odot}$ (Borthakur et al. 2010).

For ease of visualization, we show in Fig. 5 the different symbols marking the position of the galaxies, H I clumps of interest and tidal arm introduced in Fig. 4 on top of a DSS-2 red band image, along

with our WiFeS observation fields. The full extent of the different H I structures is traced with iso-contours (at a level of 2.5 mJy beam $^{-1}$) and coloured as a function of the gas velocity in Fig. 6.

Globally, the different sub-structures of the H I gas distribution in the group can be associated with the different individual galaxies. Specifically:

- (i) HCG 91a – spatially, this galaxy is coherent with the large H I structure to the south of the group. The large tidal feature detected in H I is also spatially coherent with a faint optical counterpart distinguishable in the red band DSS-2 image of the area (see Fig. 5). Kinematically however, we find a mismatch of ~ 220 km s $^{-1}$ between the optical redshift of the galaxy (6832 km s $^{-1}$; see Hickson et al. 1992) and the mean redshift of the H I structure. Although the optical redshift of HCG 91a associates the galaxy with a local H I overdensity in the PV diagram of Fig. 4, most of the H I gas spatially coherent with the galaxy (including the base of the tidal tail) is redshifted by up to ~ 400 km s $^{-1}$ with respect to the optical redshift. The H I distribution observed with the VLA (both the spatial extent and the dynamic range of the different structures) is consistent with similar observations from Barnes & Webster (2001) using the Australia Telescope Compact Array, while the optical redshift measurement of HCG 91a from Hickson et al. (1992) ($z = 0.022789$) is consistent with the redshift measurement from the 6dF Galaxy Survey data release 3 ($z = 0.022739$; see Jones et al. 2004, 2009) and with our own observations of the galaxy with WiFeS. Altogether, these observations confirm that the observed optical-radio redshift mismatch of HCG 91a is real. Here, we merely mention the existence of this redshift mismatch, and defer any further discussion to a later paper dedicated to our WiFeS observations of HCG 91a.

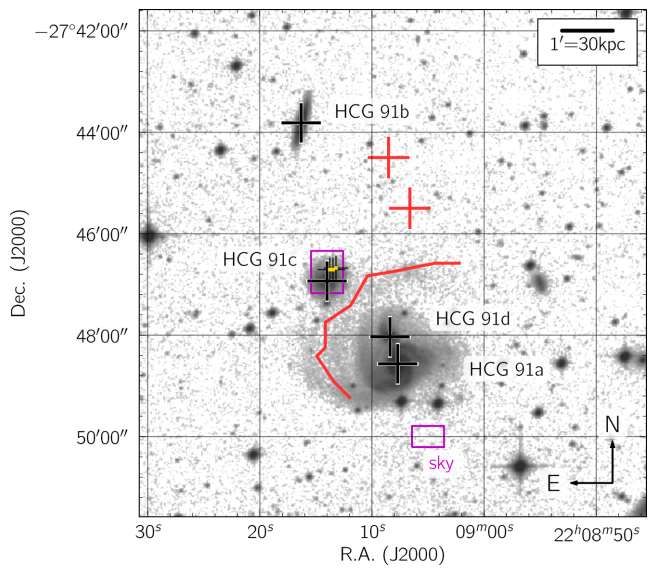


Figure 5. Red band image of HCG 91a, b, c and d from DSS-2. The image spans the same area as the position–position velocity diagram of Fig. 4 (left), of which the same markers are shown for comparison. The purple rectangles denote the footprint of our WiFeS observations of HCG 91c.

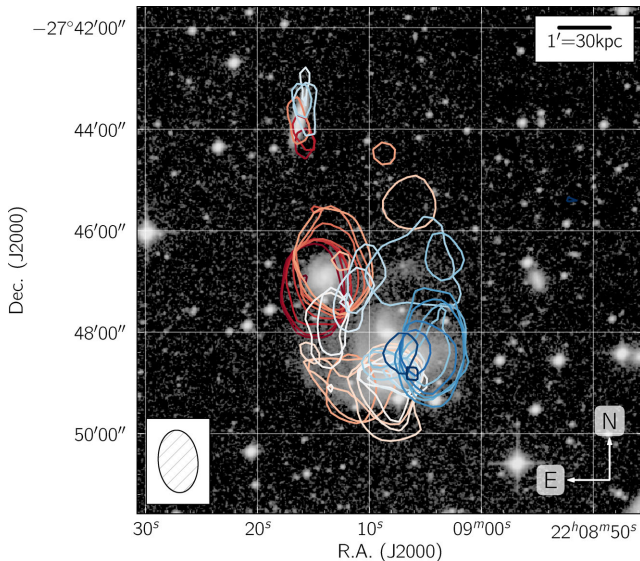


Figure 6. Red band image of HCG 91a, b, c and d from DSS-2. The image spans the same area as shown in Fig. 4 (left) and Fig. 5. Isointensity contours trace the H₁ content of the group, and are colour-coded as a function of their radial velocity, ranging from 6822.0 km s⁻¹ (dark blue) to 7405.5 km s⁻¹ (dark red), in steps of ~ 21.6 km s⁻¹. The contours are extracted from the different velocity slices of the VLA data cube and trace an intensity of 2.5 mJy beam⁻¹.

(ii) HCG 91b – a spatially compact and kinematically extended (~ 490 km s⁻¹) H₁ structure is associated with this galaxy. The large range of the H₁ kinematics is consistent with the fact that HCG 91b is seen almost edge-on.

(iii) HCG 91c – a rotating H₁ disc with a velocity range of ~ 200 km s⁻¹ (~ 7200 – 7400 km s⁻¹) is associated both spatially and kinematically with the optical counterpart of HCG 91c. We find a small kinematic offset of ~ 10 km s⁻¹ between the optical redshift of HCG 91c measured by Hickson et al. (1992) and the mean velocity of the H₁ structure. The largely undisturbed morphology of the H₁ distribution is suggesting the presence of only minimal tidal effects for this galaxy. To the north-west, two fainter H₁ sub-structures (marked with red crosses in Fig. 4) appear connected to the main gas reservoir of HCG 91c. They are also connected (less strongly) at the 1.3 mJy beam⁻¹ level to the H₁ structure associated with HCG 91b. These two H₁ clumps are located 116 arcsec ≈ 58.4 kpc and 150 arcsec ≈ 75.5 kpc from the centre of HCG 91c. They have no visible optical counterpart in the DSS-2 red band image in Fig. 5. Spatially, HCG 91c is located ~ 15 kpc to the north-east of the large tidal arm originating from HCG 91a. The H₁ gas in the tidal arm is blueshifted by 150–250 km s⁻¹ from the mean velocity of HCG 91c.

(iv) HCG 91d – this galaxy is not associated with any H₁ structure kinematically.

The large tidal feature originating from HCG 91a makes the HCG 91 compact group a *Phase 2* group in the classification of Verdes-Montenegro et al. (2001), although some of the H₁ gas is still clearly associated with the galaxies HCG 91b and HCG 91c. The H₁ reservoir associated with HCG 91c appears largely undisturbed from a kinematic point of view. The two H₁ gas clumps located to the north-west of HCG 91c may have resulted from tidal stripping, suggesting that HCG 91c is experiencing the first stages of tidal disruption via gravitational interaction. The H₁ *bridge* at the 1.3 mJy beam⁻¹ level connecting the gas reservoir of HCG 91b and HCG 91c could be seen as evidence for an ongoing interaction

between the H₁ envelopes of these two galaxies, although the exact *bridge* structure would require a higher spatial sampling to be clearly established.

4 THE GALAXY HCG 91C

Here, we describe the different characteristics of HCG 91c as seen by WiFeS and Pan-STARRS. We focus our analysis on the strong emission lines and the associated underlying physical characteristics of the ionized gas. We restrict ourselves to a description of the system, and postpone a global discussion of the different measurements until Section 5.

4.1 Spatial distribution of the stellar light

A colour-composite image of HCG 91c, constructed from the Pan-STARRS i_{P1} , r_{P1} and g_{P1} band images, is shown in Fig. 7. The same image is shown twice, with the intensity stretch adjusted to reveal the outer regions (left-hand panel) and the inner spiral structure (right-hand panel) of HCG 91c. The WiFeS mosaic footprint is traced by a dashed rectangle in the left-hand panel, and the location of R_{25} is traced by an ellipse in the right-hand panel. Specifically, $R_{25} = 26.75 \pm 3.25$ arcsec = 13.5 ± 0.2 kpc with an ellipticity of 0.91, following NED and the Third Reference Catalogue of Bright Galaxies (de Vaucouleurs et al. 1991). We note that this value is consistent with the estimate of $R_{25} = 28.45$ arcsec and an ellipticity of 0.87 from the Surface Photometry Catalogue of the ESO-Uppsala Galaxies (Lauberts & Valentijn 1989).

HCG 91c harbours a regular, tightly wrapped spiral pattern with a bright nucleus. The outer limit of the stellar disc, traced by white isocontours in the right-hand panel of Fig. 7 (extracted from the g_{P1} image) is mostly regular, with the brightness dropping the most sharply towards the SE. The spiral arms are extending (at least) 20 arcsec ≈ 10 kpc from the galaxy centre, but their brightness decreases rapidly beyond ~ 5 kpc.

The C1, C2 and C3 regions defined in Fig. 2 appear as three distinct compact features (each indicated by a white arrow in the left-hand panel of Fig. 7 for clarity). The Pan-STARRS broad-band images primarily trace the stellar content of HCG 91c, and one must use caution when comparing this view to that of the ionized gas provided by WiFeS. Nevertheless, with a diameter of ~ 6 Pan-STARRS pixels ≈ 1.5 arcsec ≈ 750 pc across, it is very likely that the optical emission associated with the C1, C2 and C3 star-forming regions is unresolved both in our WiFeS observations and in the Pan-STARRS image of HCG 91c.

4.2 Emission line maps and line ratio diagrams

We present the flux line maps for the principle optical emission lines ([O II], H β , [O III], H α , [N II], [S II]) in the spectrum of HCG 91c (before applying the extragalactic reddening correction) in Fig. 8. For comparison purposes, all the maps are shown with the same colour stretch and cuts. In each panel, the white contours at 2.2×10^{-17} erg s⁻¹ cm⁻² trace approximatively the regions with S/N ≥ 5 .

The structure of the emission from the [N II] and [S II] lines is similar to H α , although with an overall weaker intensity. There is a distinct lack of [O II] emission from the core of the galaxy, a region subject to a larger reddening (see Fig. 3). The noise level is much higher in the [O II] map, because the lines are located at the very blue end of the WiFeS spectra (in a region subject to flat-fielding problems, see Section 2.1.2). The spatial distribution of the [O III]

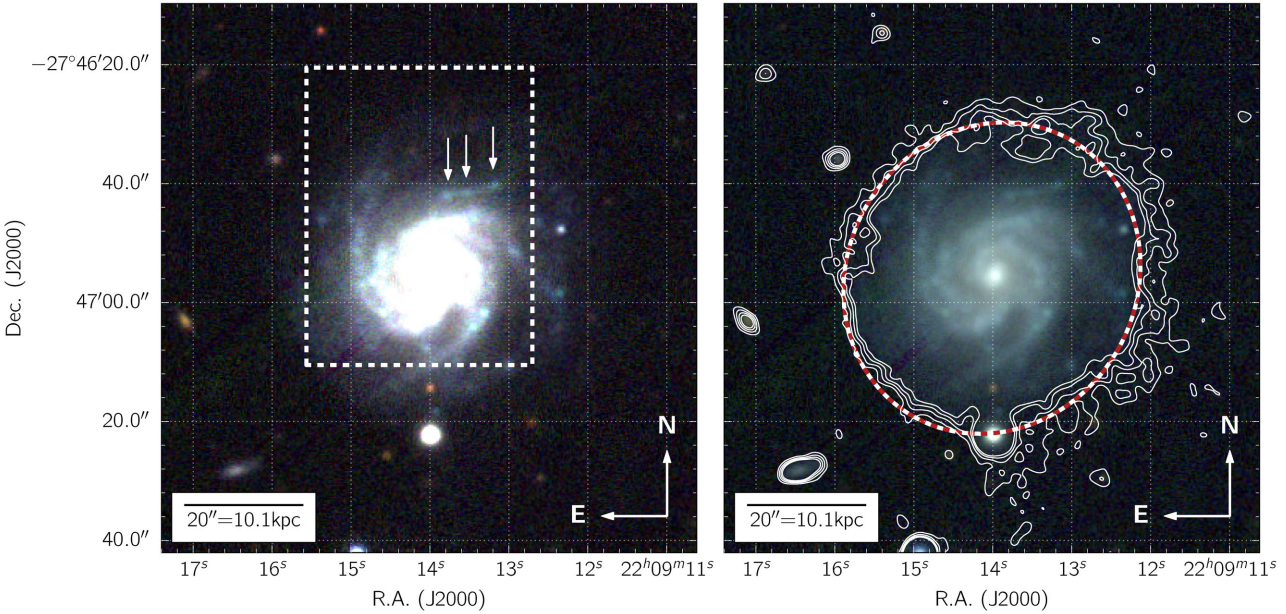


Figure 7. Colour combination of Pan-STARRS i_{P1} , r_{P1} and g_{P1} images (shown as the red, green and blue channels, respectively) of HCG 91c. The colour scheme is stretched to reveal the galaxy outskirts (left) or the inner region and spiral structure (right). The WiFeS observations footprint is marked with a dashed rectangle in the left-hand panel, along with three arrows marking the location of the C1, C2 and C3 regions. R_{25} is traced by the dashed ellipse in the right-hand panel. Also in the right-hand panel, low level isocontours constructed from a Gaussian smoothed g_{P1} band image highlight the full optical extent of HCG 91c on the sky at a distance of $\sim R_{25}$.

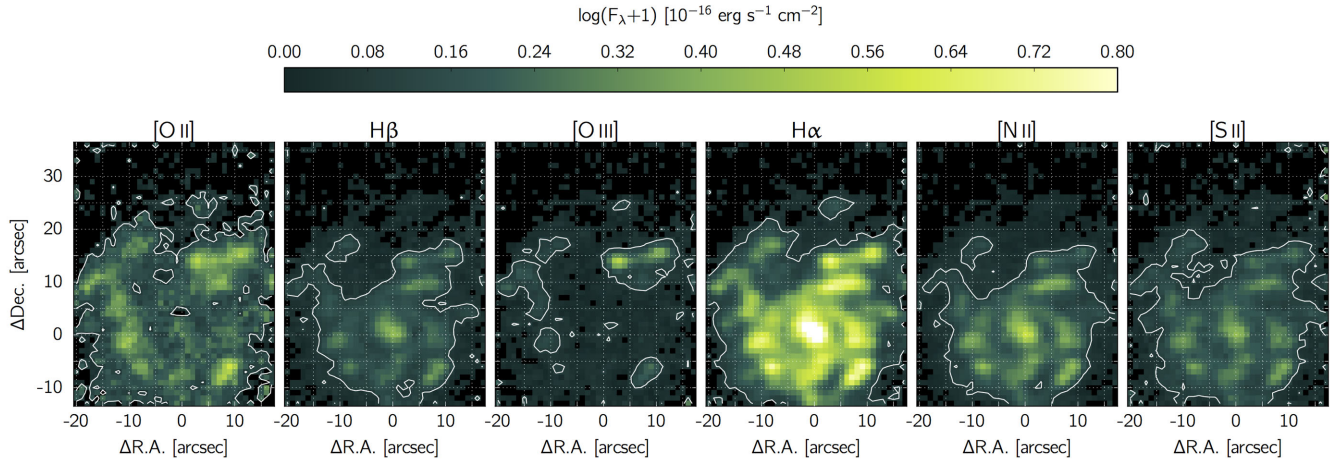


Figure 8. Maps for the different emission lines considered in this paper, shown with a uniform colour scheme and colour stretch for comparison purposes. For each line, the white contours at $2.2 \times 10^{-17} \text{ erg s}^{-1} \text{ cm}^{-2}$ approximatively trace the regions with $S/N \geq 5$.

line is distinctly different from that of $\text{H}\alpha$. The lack of emission at the core of the galaxy is reminiscent of $[\text{O II}]$, and is consistent both with a larger extinction and with a higher gas metallicity overall in the core of HCG 91c (see Section 4.3). Further out, the $[\text{O III}]$ emission is the strongest in the C1 and C3 regions. By comparison, the $\text{H}\alpha$ emission associated with the C1 and C3 regions is at a level comparable to other star-forming regions within the spiral arms.

The standard line ratio diagrams $\log [\text{N II}]/\text{H}\alpha$ versus $\log [\text{O III}]/\text{H}\beta$ and $\log [\text{S II}]/\text{H}\alpha$ versus $\log [\text{O III}]/\text{H}\beta$ for HCG 91c are shown in Fig. 9. Each 353 spaxels for which $S/N(\text{H}\alpha; \text{H}\beta) \geq 5$ and $S/N([\text{O III}]; [\text{N II}]; [\text{S II}]) \geq 2$ are shown as individual squares, colour-coded as a function of $S/N([\text{O III}])$. The first S/N selection condition results from the extragalactic reddening correc-

tion described previously. A lower S/N cut for $[\text{O III}]$, $[\text{N II}]$ and $[\text{S II}]$ is then acceptable given that both $\text{H}\alpha$ and $\text{H}\beta$ are clearly detected and strongly constrain the velocity and velocity dispersion of all the different emission lines. The colour scheme choice reflects the fact that $S/N([\text{O III}]) \geq 2$ is in all cases the *limiting condition*. The grey error bars shown in each diagram indicate the 1σ error associated with the line ratio measurements, calculated from the errors measured by LZIFU based on the variance measurements propagated through the PYWIFES data reduction pipeline.

Within the errors, the different spaxels form a well-defined sequence in both line ratio diagrams, extending 1.5 dex along the $\log [\text{O III}]/\text{H}\beta$ direction. The spaxel density along the sequence is continuous, except for a marked decrease at $\log [\text{O III}]/\text{H}\beta \approx 0$. This

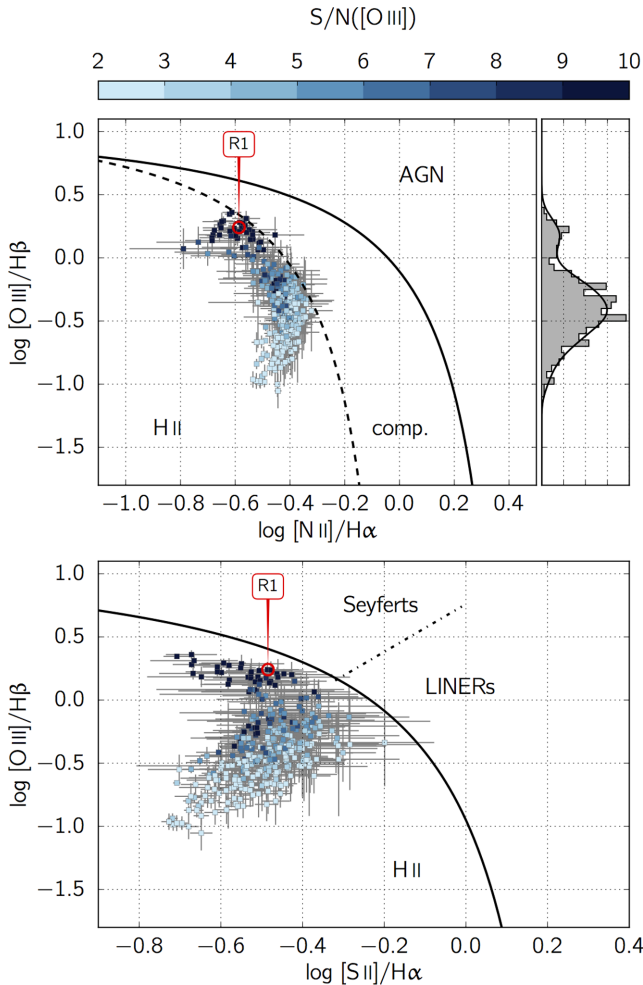


Figure 9. Standard line ratio diagnostic diagrams $\log [N\text{ II}]/H\alpha$ versus $\log [O\text{ III}]/H\beta$ (top) and $\log [S\text{ II}]/H\alpha$ versus $\log [O\text{ III}]/H\beta$ (bottom). Each spaxel with $S/N(H\alpha;H\beta) \geq 5$ and $S/N([O\text{ III}];[N\text{ II}];[S\text{ II}]) \geq 2$ are marked with squares coloured as a function of $S/N([O\text{ III}])$. The position of the R1 integrated spectra is marked with a red circle and labelled accordingly. The 1σ errors are shown in grey for each measurement. The full black lines are the maximum starburst diagnostic lines from Kewley et al. (2001), the dashed line is the starburst diagnostic line from Kauffmann et al. (2003), while the Seyferts–LINERs separation from Kewley et al. (2006) is marked as a dash-dotted line in the bottom panel. The histogram in the upper panel shows the spaxel distribution as a function of $\log [O\text{ III}]/H\beta$, while the smooth distribution (traced by the black curve) was derived by performing a kernel density estimation on the distribution of $\log [O\text{ III}]/H\beta$ values.

gap, best seen in the density histogram in the right-hand side of the upper panel of Fig. 9, is most certainly not a consequence of low S/N measurements. Indeed, spaxels on either side and across this gap in the distribution have strong oxygen emission with $S/N([O\text{ III}]) \gtrsim 6$, and are therefore clearly detected.

In Fig. 10, we show the $\log [O\text{ III}]/H\beta$ line ratio map for all 353 spaxels visible in either panel of Fig. 9. Along with the R1 region, the spaxels associated with the C1, C2 and C3 regions have $\log [O\text{ III}]/H\beta \geq 0$. They are forming the upper end of the star-forming sequence visible in the line ratio diagrams. Altogether, Figs 9 and 10 indicate an abrupt change in the physical conditions of the ionized gas between the C1, C2 and C3 regions and their immediate surroundings.

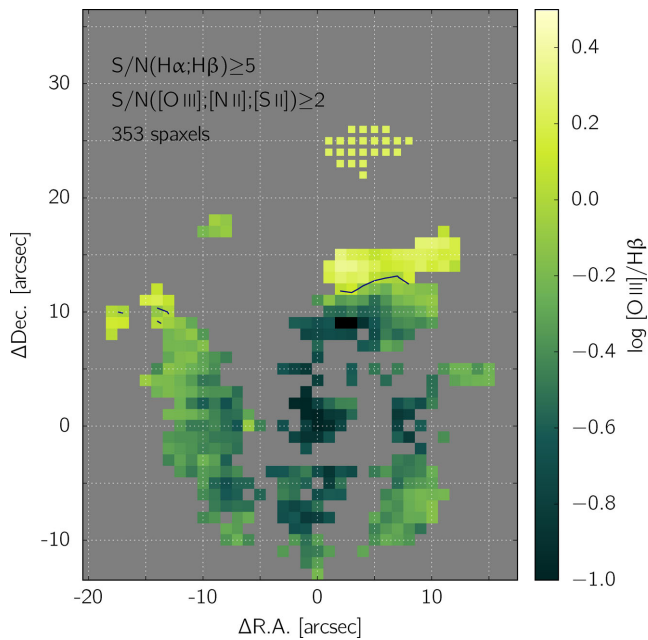


Figure 10. Map of $\log [O\text{ III}]/H\beta$ for spaxels with $S/N(H\alpha;H\beta) \geq 5$ and $S/N([O\text{ III}];[N\text{ II}];[S\text{ II}]) \geq 2$. Most spaxels with a positive ratio are located in the C1, C2 and C3 regions. The black line traces the isocontour corresponding to $\log [O\text{ III}]/H\beta = 0$.

4.3 Oxygen abundance and ionization parameters

We now delve deeper into the physics of emission line ratios, and compute oxygen-abundances and ionization parameters for each 353 spaxels with $S/N(H\alpha;H\beta) \geq 5$ and $S/N([O\text{ III}];[N\text{ II}];[S\text{ II}]) \geq 2$. The concept and the method employed here follow Dopita et al. (2014). We use the PYQZ v0.6.0 PYTHON module to compute, for each spaxel, the value of the oxygen abundance $12+\log(O/\text{H})$ and the ionization parameter $\log(q)$ (with q in cm s^{-1}). The code relies on a series of grids of photoionization models computed with MAPPINGS IV – the most recent embodiment of the MAPPINGS code (Binette et al. 1982; Dopita, Binette & Schwartz 1982; Binette, Dopita & Tuohy 1985; Sutherland & Dopita 1993; Groves, Dopita & Sutherland 2004; Allen et al. 2008) – which for a distinct set of line ratio diagrams allow us to disentangle the values of $12+\log(O/\text{H})$ and $\log(q)$ over a large parameter space ($5-0.05 Z_\odot$ and $6.5 \leq \log(q) \leq 8.5$). Among other updates, MAPPINGS IV allows for a non-Maxwellian distribution for the electron energies in the form of a κ -distribution (Nicholls, Dopita & Sutherland 2012; Dopita et al. 2013; Nicholls et al. 2013). Here, we adopt $\kappa = 20$, but we note that this choice does not significantly affect our analysis, given the limited influence of a κ distribution on the intensity of strong emission lines.

We note that for this work we have upgraded PYQZ from v0.4.0 publicly released by Dopita et al. (2013) to v0.6.0. In this latest version, PYQZ can fully propagate errors in the line flux measurements through to the estimation of the abundance and ionization parameters (but still relies on the same MAPPINGS IV models of Dopita et al. 2013). The new PYQZ v0.6.0 will be publicly released in the near future along with updated MAPPINGS IV models (Sutherland et al., in preparation), and is available *on demand* until then. For completeness, we describe in Appendix B how observational errors are propagated in this new version of PYQZ and how the final 1σ uncertainty level on the $12+\log(O/\text{H})$ and $\log(q)$ values is computed,

namely via the propagation of the full probability density function associated with each emission line measurement.

In total, eight diagnostic grids are available in PYQZ to compute the abundance and ionization parameter of a given spectrum. In principle, each of these grids can provide an estimate of $12+\log(\text{O/H})$ and $\log(q)$, which can then be combined to provide a global estimate. In practice, and for the present case, we only used the diagnostics not involving $[\text{O}\,\text{II}]$ because these emission lines are subject to flat-fielding issues (see Section 2.1.2). In addition, an inherent twist in the model grid over the region of interest for HCG 91c renders the diagram $\log([\text{N}\,\text{II}]/\text{H}\alpha)$ versus $\log([\text{O}\,\text{III}]/\text{H}\beta)$ unusable in the present case. Ultimately, we are left with just two suitable diagnostic grids: $\log([\text{N}\,\text{II}]/[\text{S}\,\text{II}])$ versus $\log([\text{O}\,\text{III}]/\text{H}\beta)$ and $\log([\text{N}\,\text{II}]/[\text{S}\,\text{II}])$ versus $\log([\text{O}\,\text{III}]/[\text{S}\,\text{II}])$.

The resulting $12+\log(\text{O/H})$ and $\log(q)$ maps for HCG 91c are shown in Fig. 11. As mentioned previously, the overall decrease of the $[\text{O}\,\text{III}]$ flux in the inner regions of HCG 91c is associated with increasing oxygen abundances. The peak oxygen abundance at the galaxy centre is $12+\log(\text{O/H}) \approx 9.25$. By comparison, the oxygen abundance of the R1 region is found to be $12+\log(\text{O/H}) \approx 8.80$. The oxygen abundance of the C1, C2 and C3 regions is of the order of 8.7–8.9. The ionization parameter map is uniform throughout the entire galaxy ($7.10 \lesssim \log(q) \lesssim 7.35$). The C1 region is a notable and the only significant departure from the mean with $\log(q) \approx 7.65$.

In Fig. 12, we construct the abundance gradient of HCG 91c as a function of the deprojected radius. Every 353 spaxels for which we derived an oxygen abundance are shown individually. The vertical error bar associated to each measurement corresponds to the error computed by PYQZ v0.6.0. To deproject the position of each spaxel in the disc of HCG 91c, we assume an ellipticity $b/a = 0.8 \pm 0.08$ (measured manually from the r_{PI} image of HCG 91c from Pan-STARRS), and a PA = 40° west-of-north (measured from the rotation map of HCG 91c, see Section 4.4). This PA is in disagreement with the PA available in NED based on near-IR images from 2MASS (Skrutskie et al. 2006) of 5° west-of-north, but is in good agreement with the PA derived from optical images from the Surface Photometry Catalogue of the ESO-Uppsala Galaxies (Lauberts & Valentijn 1989) of 46° west-of-north. The horizontal error bar associated with each measurement corresponds to an estimated 10 per cent measurement error on the ellipticity. We assumed the centre of the galaxy to be located at the position [0,0], coincident with the peak $\text{H}\alpha$ emission, which given the seeing conditions is also consistent with the kinematic centre of the galaxy, as described in the next section.

As illustrated in the top panel of Fig. 12, a linear fit to the full set of data points fails to properly match the outer regions of the disc. It is clear from Fig. 11 that our sampling of the outer regions of the disc (where $12+\log(\text{O/H}) \leq 8.92$) is poor, and largely composed of the C1, C2 and C3 regions. Hence, the global gradient fit is largely influenced by the spaxels in the inner regions of HCG 91c. In the middle panel of Fig. 12, we use a linear *broken* fit to better reproduce the trend in the oxygen abundance throughout HCG91c. The fit is broken at 4.5 kpc from the galaxy centre – the approximate radius at which the oxygen abundance gradient appears to steepen. An *inner gradient* is derived from spaxels in the Zone 1 (Z1; radius < 4.5 kpc, $12+\log(\text{O/H}) > 8.92$), while an *outer gradient* is derived from spaxels in the Zone 2 (Z2; radius ≥ 4.5 kpc, $12+\log(\text{O/H}) > 8.92$), and forced to match the inner gradient at 4.5 kpc. The respective slopes of the different gradients are compiled in Table 2. All oxygen abundance gradients were derived using the

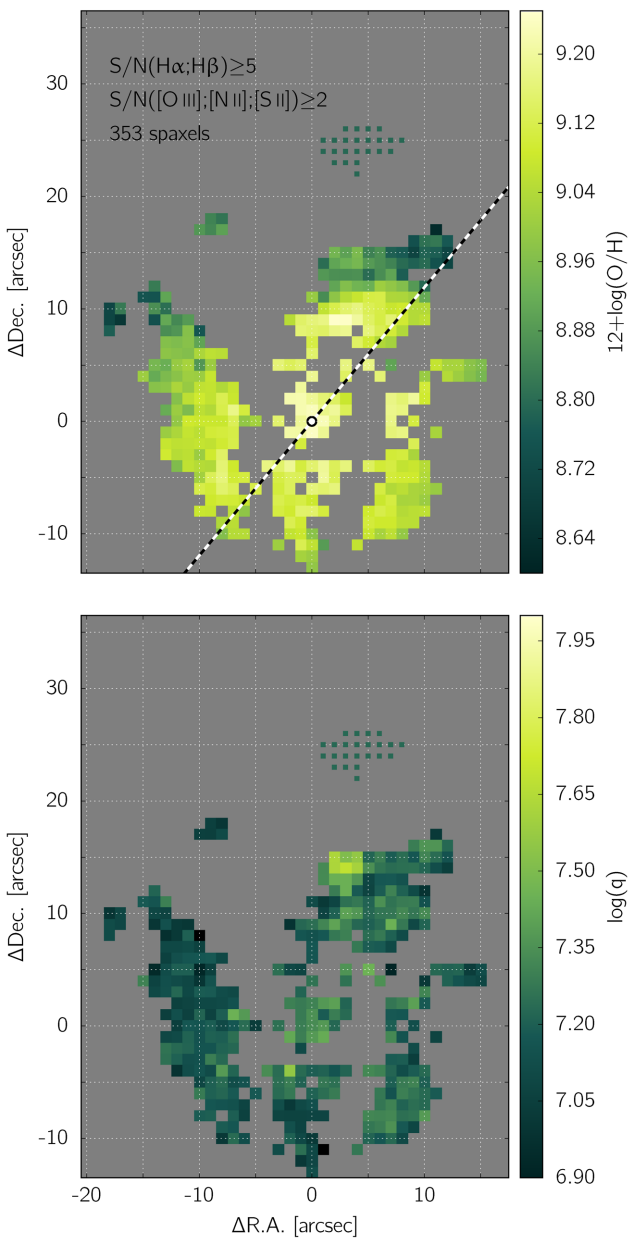


Figure 11. Gas phase oxygen abundance (top) and ionization parameter (bottom) measured with the PYQZ PYTHON module for all spaxels with $S/N(\text{H}\alpha:\text{H}\beta) \geq 5$ and $S/N([\text{O}\,\text{III}];[\text{N}\,\text{II}];[\text{S}\,\text{II}]) \geq 2$. In the top panel, the dashed line traces the major axis of HCG 91c with a PA of 40° deg west-of-north (see Section 4.4).

Orthogonal Distance Regression routines inside the SCIPY module in PYTHON.⁵

A series of spaxels beyond 7 kpc from the galaxy centre remain below the best-fitting outer gradient by ~ 0.15 dex. In the bottom panel of Fig. 12, we show in black the spaxels located within 3 arcsec from the galaxy's major axis visible in Fig. 11. These spaxels trace an abrupt drop in the oxygen abundance of ~ 0.2 dex at 7 kpc from the galaxy centre over a distance of 1 kpc = 2 WiFeS spaxels.

⁵ <http://docs.scipy.org/doc/scipy/reference/odr.html>, accessed on 2015 February 12.

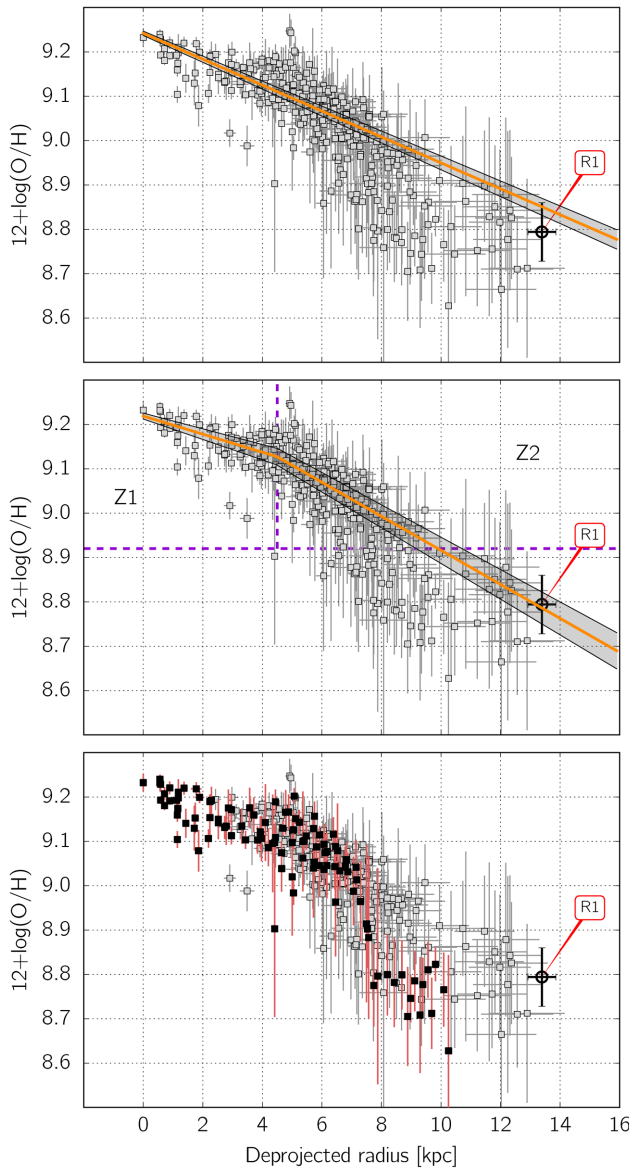


Figure 12. Oxygen abundance gradient in HCG 91c. Each 353 spaxels for which $12+\log(\text{O}/\text{H})$ could be measured (see Fig. 11) are shown individually with their associated 1σ errors. The galaxy centre, taken to be the peak of the $\text{H}\alpha$ emission line flux map, is at the position [0,0] (see Fig. 2). A PA = 40° and an ellipticity $b/a = 0.8$ are assumed to deproject the radius of each spaxel within the disc of HCG 91c. The horizontal error bars correspond to a measurement error of 10 per cent of the ellipticity. The vertical error bars are the error computed by pyoz v0.6.0. The linear best fit (and associated 1σ error) to all the spaxels is shown in the top panel. A broken linear fit, better matching the outer regions of the galaxy, is shown in the middle panel. In the bottom panel, the spaxels located within 3 arcsec from the galaxy's major axis (shown in Fig. 11) are drawn in black with their associated errors in red. They reveal the abrupt drop of ~ 0.2 dex in oxygen abundance at ~ 7.5 kpc to the north-west of the galaxy centre: the location of the C1, C2 and C3 star-forming regions.

This sharp oxygen abundance decrease is essentially unresolved (spatially) in our data set, so that its true nature (physical discontinuity in the oxygen abundance or sharp but continuous decrease) remains uncertain. It is however clear that the intensity of the oxygen abundance drop at 7 kpc is inconsistent with any linear gradient extrapolated from the inner regions of HCG 91c.

Table 2. Characteristics of the different oxygen abundance gradients presented in Fig. 12.

Gradient	Fitted region(s)	Slope (dex kpc $^{-1}$)	Zero-point
Global fit	All	-0.029 ± 0.001	9.242 ± 0.005
Inner fit	Z1	-0.020 ± 0.003	9.219 ± 0.007
Outer fit	Z2	-0.038 ± 0.002	9.300 ± 0.011

We deliberately use only spaxels in the zone Z2 to derive the best-fitting linear outer gradient, as we detect spaxels with $12+\log(\text{O}/\text{H}) > 8.92$ for (almost) all azimuths beyond a radius of 4.5 kpc. Our sampling of less enriched gas is much less uniform, so that including all the spaxels with $12+\log(\text{O}/\text{H}) < 8.92$ in the outer gradient fit would wrongly bias it towards the C1, C2 and C3 regions of which the abundances (as illustrated in the bottom panel of Fig. 12) are clearly inconsistent with a linear gradient. Although the outer gradient is derived solely from the Z2 spaxels, we note that its slope nevertheless matches some of the outer regions of HCG 91c, including the R1 region.

In the top panel of Fig. 13, we colour-code the different spaxels as a function of their associated S/N($[\text{O III}]$). Most spaxels lying in

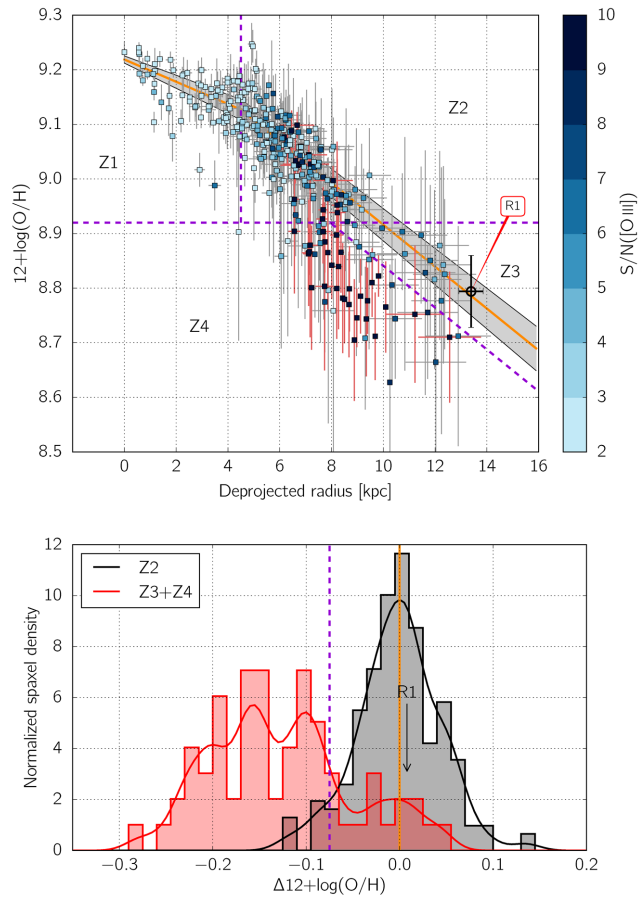


Figure 13. Top: same as the middle panel of Fig. 12, but with the individual spaxels coloured as a function of S/N($[\text{O III}]$). The diagram is divided in four gradient zones (labelled Z1–Z4) based on the overall trend morphology. For clarity, errors for spaxels with $\text{S/N}([\text{O III}]) \geq 9$ are shown with thicker dark-red lines. Bottom: histogram and associated smooth distribution of the oxygen abundance offset from the best-fitting outer gradient, for spaxels in the Z2 zone (black) and in the Z3+Z4 zones (red).

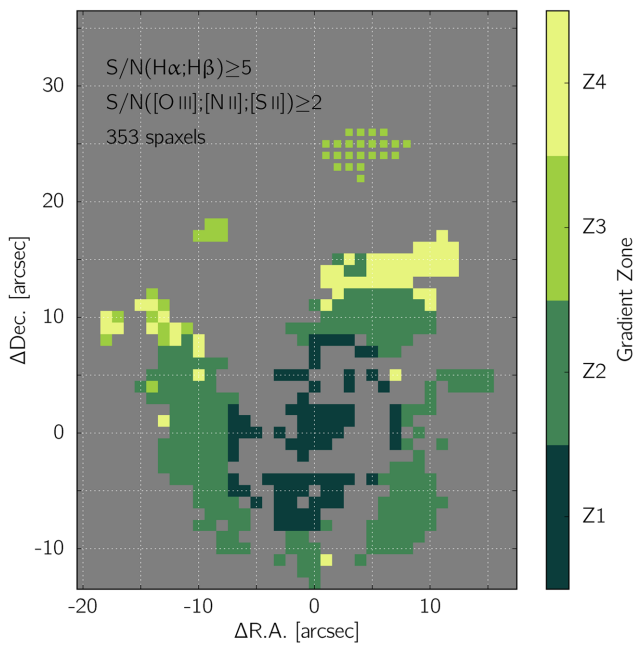


Figure 14. Spatial distribution of the spaxels in the different gradient zones Z1 to Z4 defined in Fig. 13.

the Zone 4 (Z4; $12+\log(\text{O/H}) < 8.92$, $12+\log(\text{O/H})$ more than 0.075 dex below the best-fitting outer gradient based on the Z2 spaxels) are clearly detected, and their errors (shown in dark red for clarity) place them 1σ – 2σ below our best-fitting outer gradient. Their offset in oxygen abundance is best seen in the figure’s bottom panel, showing the distribution of oxygen abundances for all spaxels in the zones Z2 and Z3+Z4. While some spaxels below $12+\log(\text{O/H}) = 8.92$ are consistent with the linear gradient estimate based on the Z2 spaxels out to 13 kpc (i.e. spaxels in the zone Z3), most lie 0.15–0.3 dex lower (in the zone Z4).

Most spaxels in the zone Z4 belong to the C1, C2 and C3 regions, as illustrated in Fig. 14. It can be noted that as the C1, C2 and C3 regions are located along or near the PA of HCG 91c, their deprojected radii are not subject to large uncertainties. The Z3 spaxels are on the other hand all located in the outer regions of the spiral arm extending northwards from the left-hand side of HCG 91c. Especially, the lack of S/N in the $[-10; 15]$ area (see Fig. 11) appears consistent with the lack of detection of Z3 spaxels at a radius of 10–11 kpc.

4.4 Kinematics of the ionized gas

In Fig. 15, we show the ionized gas velocity map (centre) and velocity dispersion (right) of HCG 91c. In the left-hand panel, we show the H α intensity map overlaid with the isovelocity contours. We use the freely available PYTHON routine `FIT_KINEMATIC_PA` from M. Cappellari⁶ to measure the PA of HCG 91c from its gas kinematics: $\text{PA} = 40 \pm 4$ deg west-of-north. This routine (originally written in `IDL`) was used extensively by Cappellari et al. (2007) and Krajnović et al. (2011), and is described in appendix C of Krajnović et al. (2006). The $\text{PA} = 40^\circ$ (black and white dashed line) direction and the galaxy centre (white dot) used to construct the abundance

gradient of HCG 91c shown in Fig. 13 are shown in the left-hand and middle panel of Fig. 15 for completeness.

The kinematic signature of the gas in HCG 91c is consistent with regular rotation. The quoted velocities assume a rest frame velocity of 7319 km s^{-1} ($z = 0.024414$; Hickson et al. 1992). We find an overall asymmetry between the redshifted and blueshifted sides that could be reconciled if the rest-frame velocity was reduced by 11 km s^{-1} to 7308 km s^{-1} (as measured by `FIT_KINEMATIC_PA`). This offset would also help reconcile the optical redshift of HCG 91c with the H i kinematic of the galaxy measured by the VLA (see Section 3).

The velocity dispersion of the ionized gas is throughout the entire disc of HCG 91c ranging from ~ 20 to 40 km s^{-1} . Accounting for the thermal broadening of the lines ($\sigma_{\text{Th}} \approx 13(T/10^4)^{0.5} \text{ km s}^{-1}$ for the hydrogen lines, see Osterbrock 1989), this corresponds to an intrinsic velocity dispersion range of ~ 15 – 38 km s^{-1} . The largest velocity dispersions are found towards the galaxy centre, and are most certainly influenced by beam smearing, given the seeing conditions during our observations (1.2–1.5 arcsec). No significant increase of the velocity dispersion is detected towards the C1, C2 and C3 clumps.

We detect some deviations from a regular rotation signature at and around the positions [5, 15] to [12, 12] – the location of the C1, C2 and C3 regions. Specifically, the C1, C2 and C3 regions are redshifted from (i.e. are lagging behind) the regular rotation of the galaxy by 5 – 10 km s^{-1} . We recall that the error associated with the spectral calibration of the red WiFeS data cube is of the order of 0.05 \AA (see Section 2.1.2 and Childress et al. 2014b) or 2.3 km s^{-1} at H α , so that a 5 – 10 km s^{-1} offset corresponds to a 2σ – 3σ detection. The fact that the kinematic distortion is extended and tracks the bright spaxels distribution of the C1, C2 and C3 regions suggests that the distortion is real, although a greater spectral resolution and finer spatial sampling would be beneficial to confirm its existence.

To further quantify the distortions of the velocity map of HCG 91c associated with the C1, C2 and C3 star-forming regions, we construct two PV diagrams. We choose the projection axis to be oriented (a) along the galaxy’s PA and (b) along an axis rotated by 12° counter-clockwise from the galaxy’s major axis. In both cases, we set the zero-point at the galaxy centre and add 11 km s^{-1} to the measured velocities to correct the global kinematic asymmetry mentioned previously. The value of 12° bears no special significance other than ensuring that the second axis passes through the C1–C2–C3 complex of star-forming regions. The resulting PV diagrams are shown in Fig. 16. Every spaxel within 3 and 1 arcsec (respectively) from the two projection axis and with $\text{S/N}(\text{H}\alpha) \geq 5$ for which the line velocity can be measured accurately is shown as an individual red square (redshifted side of the galaxy) or a blue diamond (blueshifted side of the galaxy), as a function of its (projected) distance along the PV axis.

Along the major axis of the galaxy, after a linear increase out to ~ 2 arcsec, the slope of rotation velocity decreases and remains consistent between the red- and blueshifted sides out to ~ 12 arcsec. While the redshifted gas velocity flattens out at $\sim 75 \text{ km s}^{-1}$ beyond 12 arcsec, the blueshifted gas increases up to $80 \pm 3 \text{ km s}^{-1}$ beyond 22 arcsec. Assuming an ellipticity for HCG 91c of 0.8 ± 0.08 , we find the absolute rotation velocity of the gas at a radii greater than 11 kpc to be $100 \pm 11 \text{ km s}^{-1}$.

A noticeable feature of the top diagram is the kinematic behaviour of the blueshifted gas from 12 to 20 arcsec. As the magnified inset diagram in Fig. 16 illustrates, two velocity ‘branches’ separated by 5 – 10 km s^{-1} at the 1σ – 2σ level exist in this range. Especially, the ‘bottom’ branch corresponds to spaxels in the C3 region, and is

⁶ <http://www-astro.physics.ox.ac.uk/~mxc/software/>, accessed on 2015 February 12.

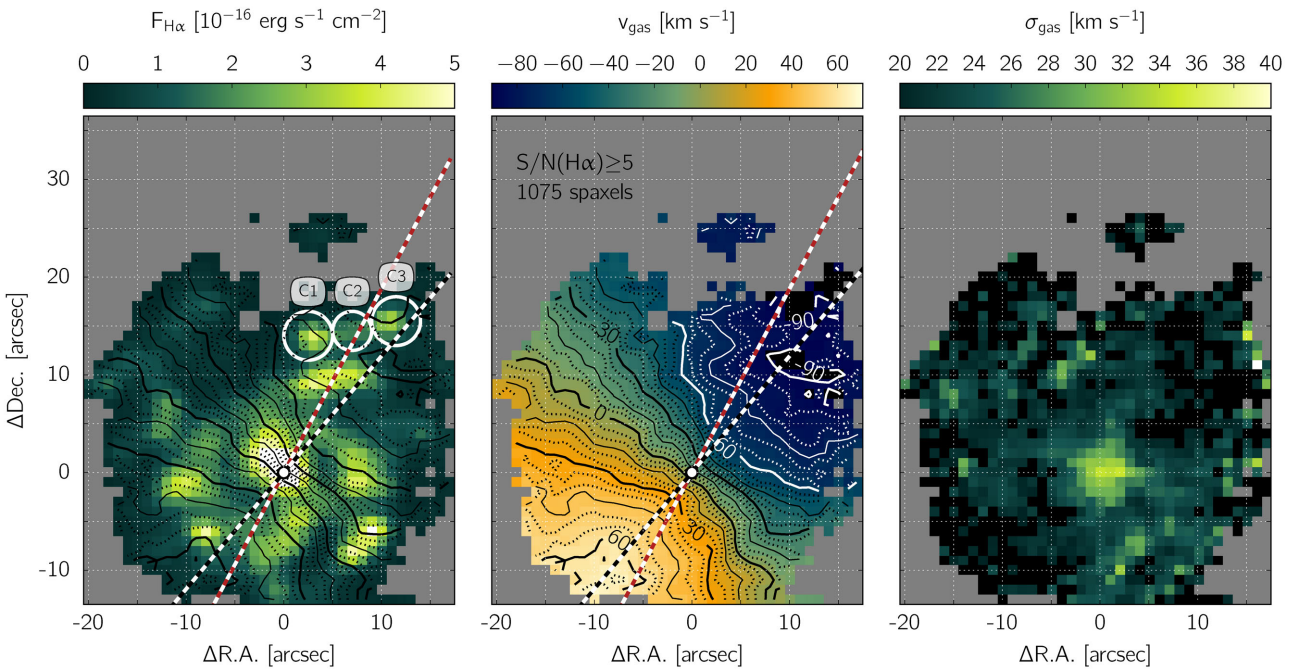


Figure 15. Velocity (centre) and velocity dispersion (right) maps of HCG 91c, for all spaxels with $S/N(H\alpha) \geq 5$. Isovelocity contours are shown in the middle panel, and are also overlaid over the $H\alpha$ flux map of HCG 91c is the left-hand panel. In the left-hand and middle panel, the centre of the galaxy (traced by the peak $H\alpha$ line flux) is marked with a white circle, and the black and white dashed line traces the principal axis of HCG 91c ($PA = 40^\circ$ west-of-north). The dark-red and white dashed line is rotated by 12° counter-clockwise from the galaxy's major axis, and is designed to pass through the C1–C2–C3 complex of star-forming regions. The PV diagrams in Fig. 16 are extracted along these two directions. For the isovelocity contours, the thick full lines are spaced by 30 km s^{-1} , the thin full lines are spaced by 15 km s^{-1} and the dashed lines are spaced by 5 km s^{-1} .

the signature of the lag of the C3 star-forming region mentioned previously. The velocity lag of the C1, C2 and C3 complex of star-forming regions is best seen in the bottom panel of Fig. 16, in which the blue velocity curve decrease by $\sim 5\text{--}10 \text{ km s}^{-1}$ at 16 arcsec from the galaxy centre (i.e. at the location of the C2 star-forming region).

Spiral galaxies in compact groups have been observed to host a wide range of rotation signatures with sometimes large asymmetries and/or perturbations (see e.g. Rubin, Hunter & Ford 1991). As compact groups favour strong gravitational interactions between galaxies, the existence of small perturbations in the velocity field of HCG 91c (located inside a compact group) is in itself not surprising. Of interest however is the fact that the star-forming regions with localized lower oxygen abundances are associated with localized kinematic anomalies. This abundance–kinematic connection indicates that both the gas *composition* and *motion* in the C1, C2 and C3 star-forming regions are inconsistent with their immediate surroundings.

4.5 Star formation rate

We can convert the $H\alpha$ line flux of each spaxel in our WiFeS mosaic (see Fig. 2) into a star formation rate ($SFR_{H\alpha}$) following the recipe of Murphy et al. (2011) derived using STARBURST99 (Leitherer et al. 1999) and assuming a Kroupa (2001) initial mass function (IMF):

$$SFR_{H\alpha} = 5.37 \times 10^{-42} \frac{L_{H\alpha}}{\text{erg s}^{-1}}, \quad (1)$$

where $L_{H\alpha}$ is the total $H\alpha$ luminosity, derived from our measured dereddened fluxes per spaxel and given the assumed distance to HCG 91c of 104 Mpc. This recipe results in an SFR 68 per cent of what would be derived using the Kennicutt (1998) formula, largely

because of differences in the assumed IMF characteristics (Calzetti et al. 2007; Kennicutt & Evans 2012). The resulting SFR map of HCG 91c is shown in Fig. 17, where only the 530 spaxels with $S/N(H\alpha; H\beta) \geq 5$ and the R1 region that were corrected for extra-galactic reddening are shown. We note that our spatial resolution of $0.5 \text{ kpc arcsec}^{-1}$ is similar to the scale of the star-forming complexes studied by Murphy et al. (2011), so that issues associated with using a ‘mean’ $H\alpha$ -to-SFR conversion factor on small scales does not apply in our case (see Murphy et al. 2011; Kennicutt & Evans 2012).

As expected from the $H\alpha$ emission line map, star formation activity in HCG 91c is most intense in the central region of the galaxy, with additional hotspots along the spiral arms. The total $SFR_{H\alpha}$ for HCG 91c (summed from all the spaxel with $S/N(H\alpha; H\beta) \geq 5$ and the R1 region) is $2.10 \pm 0.06 \text{ M}_\odot \text{ yr}^{-1}$. This value is in excellent agreement with the estimated $2.19 \text{ M}_\odot \text{ yr}^{-1}$ from Bitsakis et al. (2014) based on a full SED⁷ fitting of the integrated light of HCG 91c.

Assuming a total stellar mass $M_* = 1.86 \times 10^{10} \text{ M}_\odot$ for HCG 91c (Bitsakis et al. 2014), we obtain an $sSFR = 1.13 \pm 0.05 \times 10^{-10} \text{ yr}^{-1}$. This is comparable to the lowest $sSFR$ measured by Tzanavaris et al. (2010) in 21 star-forming HCG galaxies from their UV and IR colours, but well within the distribution of $sSFR$ reported by Plauchu-Frayn et al. (2012) for ~ 50 late-type galaxies (SBc and later) in compact groups using full optical spectrum fitting with stellar population synthesis models. In fact, HCG 91c is extremely consistent with the SFR versus M_* and $sSFR$ versus M_* relations constructed from the SDSS and GAMA data sets for z

⁷ Spectral Energy Distribution.

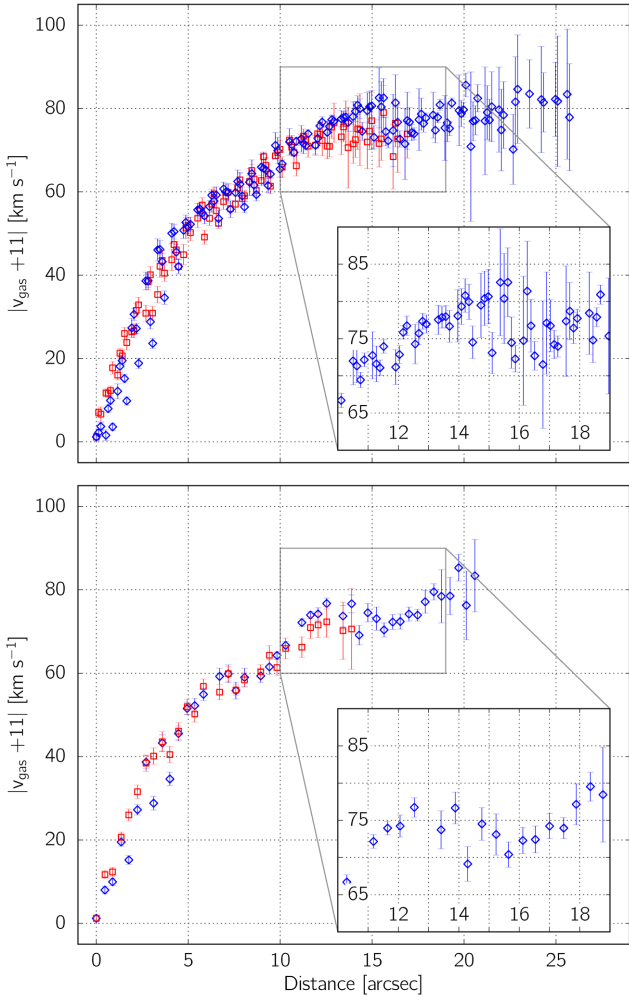


Figure 16. Top: PV diagram of the velocity map shown in Fig. 15, extracted along the axis passing through the galaxy centre and with PA = 40° west-of-north (shown with a black and white dashed line in Fig. 15). Each spaxel within 3 arcsec of the axis and with $S/N(H\alpha) \geq 5$ is shown as a red square (redshifted side of HCG 91c) or a blue diamond (blueshifted side of HCG 91c). A correction of 11 km s $^{-1}$ was added to the velocity of each spaxel to correct the global kinematic asymmetry detected in the velocity field. Bottom: idem, but for spaxels with $S/N(H\alpha) \geq 5$ located within 1 arcsec from an axis rotated by 12° counter-clockwise from the galaxy's major axis (traced with a dark-red and white dashed line in Fig. 15).

< 0.1 star-forming galaxies by Lara-López et al. (2013). For reference, we list in Table 3 the different characteristics of the C1, C2 and C3 regions, whilst their integrated spectra are presented in Fig. 18.

5 DISCUSSION: THE PECULIAR STAR-FORMING REGIONS OF HCG 91C

By and large, HCG 91c appears as a rather unremarkable star-forming spiral galaxy. It hosts regular SFRs throughout its disc comparable to other similar galaxies in the field, and an overall regular rotation (as traced by the ionized gas). This galaxy also hosts a linear oxygen abundance gradient out to ~ 4.5 kpc, which then breaks to a steeper linear gradient. The H α gas distribution around the galaxy traced by the VLA is largely undisturbed. The cold dust contours measured by *Herschel/SPIRE* at 250 μ m display

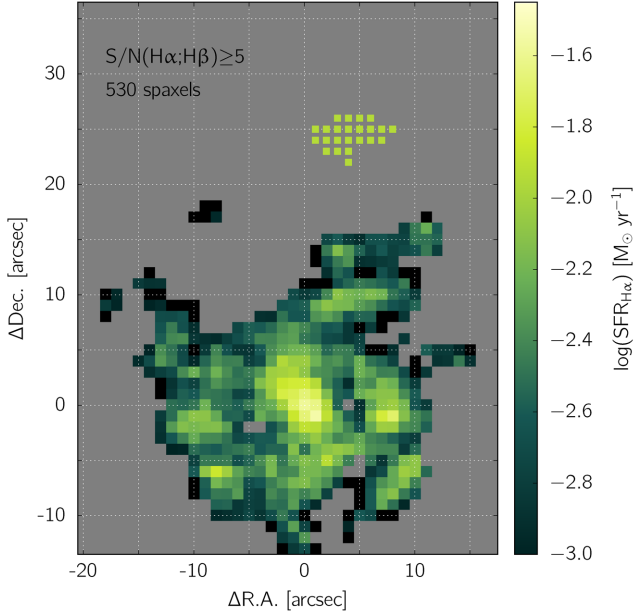


Figure 17. SFR derived from the H α flux, for all spaxel corrected for extragalactic reddening. The galaxy centre is the most active region, and the spiral structure is also visible. Localized enhancements of the SFR are detected in the C1, C2 and C3 regions.

Table 3. Main integrated characteristics of the C1, C2 and C3 star-forming regions.

Region	C1	C2	C3
$\langle \Delta R.A. \rangle$ (arcsec)	3.2	7.0	10.5
$\langle \Delta Dec. \rangle$ (arcsec)	13.5	13.5	15.3
v_{gas} (line of sight) (km s $^{-1}$)	7245 ± 4	7236 ± 3	7230 ± 4
σ_{gas} (km s $^{-1}$)	21 ± 2	20 ± 2	20 ± 2
$F(H\alpha)$ (10^{-16} erg s $^{-1}$ cm $^{-2}$)	64.0 ± 8.9	23.8 ± 6.0	49.6 ± 9.0
$SFR_{H\alpha}$ (10^{-2} M $_{\odot}$ yr $^{-1}$)	4.4 ± 0.6	1.7 ± 0.4	3.4 ± 0.6
$L_{H\alpha}$ (10^{39} erg s $^{-1}$)	2.1 ± 0.3	0.8 ± 0.2	1.6 ± 0.3

a high degree of azimuthal symmetry (Bitsakis et al. 2014). Mendes de Oliveira et al. (2003) report that HCG 91c is an outlier with respect to the *B*-band Tully–Fisher relation, in that its absolute *B*-band magnitude M_B is 2 mag brighter than expected from its rotation velocity, and concluded (also based on the two distinct kinematic components reported by Amram et al. 2003) that HCG 91c may be the result of a merger. We disagree with this picture after finding no evidence for the existence of multiple emission line component in our WiFeS data set. Furthermore, the clear and regular spiral structure detected with WiFeS and Pan-STARRS strongly argues against the merger scenario, and so is the regular photometric profile of the disc (already noted by Mendes de Oliveira et al. 2003).

Altogether, these characteristics suggest that HCG 91c has not (yet) strongly interacted gravitationally with the other galaxy members of HCG 91. The presence of faint, extended H α gas to the

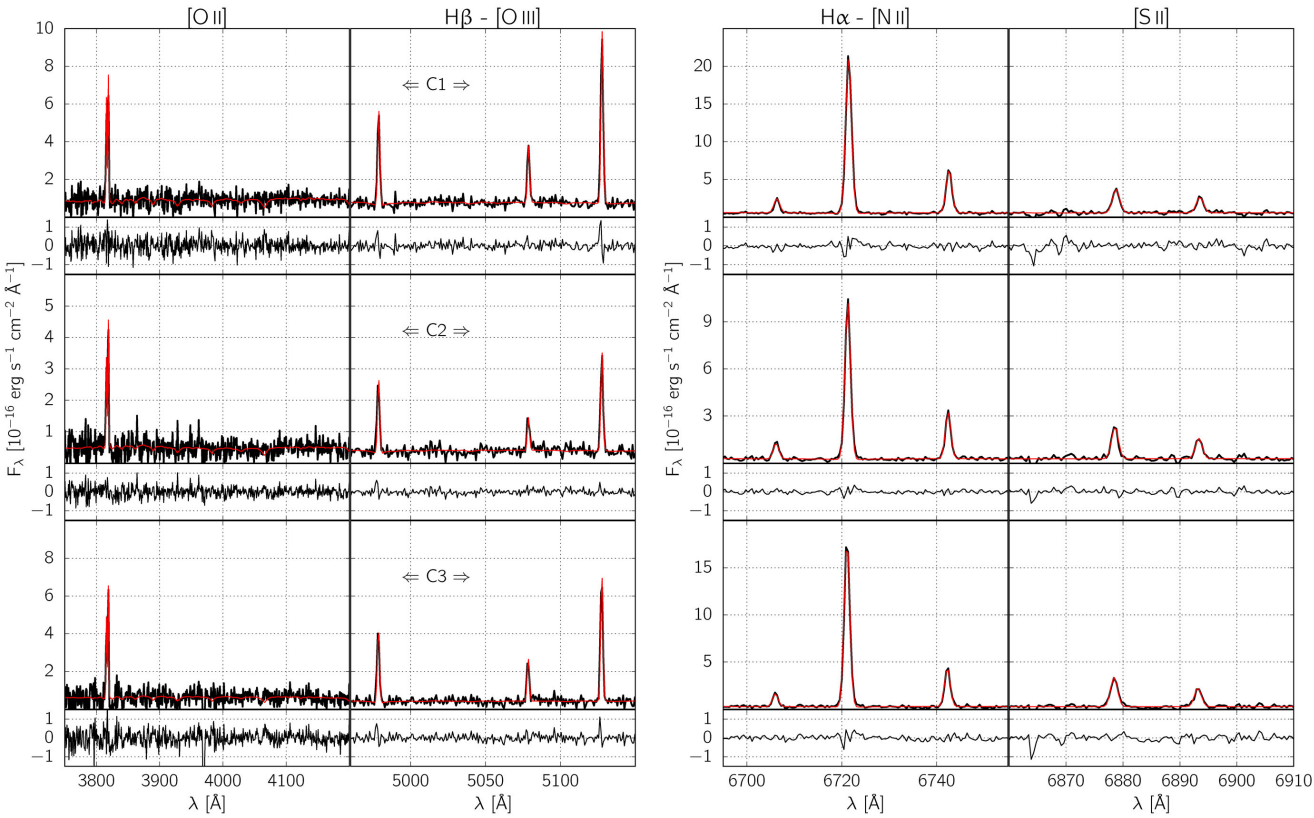


Figure 18. Raw integrated spectra (black) and LZIFU fit (red) of the C1, C2 and C3 star-forming regions. The dominant emission lines present in each panel are labelled on top of each column for clarity.

north-west of the main H₁ reservoir (see Fig. 6) suggests that HCG 91c may be caught in the very early stage of its interaction with the group. We note that the isointensity contours tracing the optical extent of the stellar disc of HCG 91c (see Fig. 7) reveal a sharp intensity drop to the south-east, but a smoother and more irregular boundary to the west and north-west, in the direction of the kinematic asymmetries and H₁ clumps.

Beside these large-scale features, we found abundance and kinematic *anomalies* (at the 1σ – 2σ level) at the location of the C1, C2 and C3 star-forming regions. Our emission line analysis reveals an abrupt change in the physical condition of the ionized gas between these star-forming regions and their immediate surroundings. They are comparatively more metal-poor by 0.15 dex, and the C1 region hosts the largest value of the ionization parameter in the disc of HCG 91c with $\log(q) \approx 7.65$. Such large values of $\log(q)$ can be explained by a very young age of the associated star-forming region (<0.5 Myr), a low-pressure environment ($\log(P/k) \approx 4\text{--}5 \text{ cm}^{-3} \text{ K}$), or both (Dopita et al. 2006). We also find evidence that the gas in the C1, C2 and C3 regions may be lagging behind the rotation of the disc by 5–10 km s^{−1}.

The lack of S/N is our WiFeS observations beyond 7 kpc from the galaxy centre hinders us from assessing the detailed behaviour of the oxygen abundance gradient at these large radii. It is clear that the oxygen abundance of the C1, C2 and C3 regions are clearly inconsistent with a linear gradient extrapolated from the inner regions of the galaxy (see Fig. 12). On the other hand, the oxygen abundances along the spiral arm extending northwards from the top-left of HCG 91c are found to be consistent with the extrapolated linear oxygen abundance gradient. This suggests that the oxygen abundance drop associated with the C1, C2 and C3 star-forming

regions is localized to these locations, rather than indicative of a uniform drop in the abundance gradient for all azimuths. Determining whether the C1, C2 and C3 star-forming regions are unique, or whether more star-forming regions in the outer regions of HCG 91c display similar (localized) abrupt decrease in oxygen abundances will require deeper follow-up observations (see Section 5.3).

5.1 Origin of the fuel for star formation

How can we explain these localized, anomalous C1, C2 and C3 star-forming regions? Their comparatively lower oxygen abundance (i.e. the presence of less enriched gas) leads us to formulate three possible scenarios to explain their origin:

- (a) the accretion of a smaller, nearby satellite system,
- (b) gas inflow on to the disc of HCG 91c from the galaxy halo, and
- (c) the infall and collapse of pre-existing neutral gas clouds at the disc–halo interface of HCG 91c.

For clarity, we discuss each of these scenarios separately.

5.1.1 Satellite accretion

The accretion of a nearby dwarf galaxy could possibly explain the lower metallicity of the C1, C2 and C3 regions. Lower metallicity dwarf galaxies have been detected around the Milky Way and M31, and the presence of large-scale stellar streams implies the ongoing accretion and tidal stretching of some of these systems (e.g. Belokurov et al. 2006; Richardson et al. 2011). The apparent on-sky alignment of the C1, C2 and C3 regions (see Fig. 7) is certainly

suggestive of a *physical* connection. Such a physical connection could then be explained by a tidally disrupted structure. However, the gas kinematic implies difficulties for this scenario. The observed lag of $5\text{--}10 \text{ km s}^{-1}$ is small compared to typical infall velocities of streams in the halo of M31 and around the Milky Way. Although not impossible, this scenario would require a very specific set of circumstances between the galaxy's orientation, the accretion trajectory, and our point of view to result in the small velocity lag of the C1, C2 and C3 star-forming regions.

5.1.2 Gas inflow from the galaxy halo

The spatial and kinematic structure of the H_I gas associated with HCG 91c certainly support the idea that this galaxy's halo (still) contains a gravitationally bound gas reserve. Under these circumstances, the lower oxygen abundance of the C1, C2, and C3 regions could be explained if less enriched and unstructured material from the halo is infalling on to the disc, and fuelling localized star formation activity. The small velocity lag and the low velocity dispersion of the gas in the C1, C2 and C3 regions would suggest a slow infall velocity. Yet, the lack of any detectable enhancement of the velocity dispersion in the C1, C2 and C3 regions compared to other star-forming regions in the disc of HCG 91c remains puzzling. The exact triggering mechanism for the gas infall also remains an open question, but the presence of nearby galaxies and their gravitational fields appear as a likely source of perturbations.

5.1.3 Infalling and collapsing gas clouds at the disc–halo interface

In the halo of the Milky Way, there exists a complex mix of gas in different phases, including molecular and neutral hydrogen (Putman, Peek & Joung 2012). Part of this gas is located in a series of compact clouds with a wide range of kinematics (Saul et al. 2012). Some of these clouds have measured velocities largely inconsistent with galaxy rotation, and are usually referred to as *high-velocity clouds* (HVCs, see e.g. Wakker & van Woerden 1997). By comparison, *intermediate-velocity clouds* (IVCs, Wakker 2001) also have velocities inconsistent with galactic rotation, but less so than HVCs. In fact, there exists a wide range of H_I cloud characteristics in the Milky Way's halo, some of which are found to be corotating with the disc (see Kalberla & Kerp 2009, and references therein). There also exists diffuse H_I gas in the halo of the Milky Way which displays a vertical lag in its rotation velocity with respect to the disc of the order of $15 \text{ km s}^{-1} \text{ kpc}^{-1}$ (Marasco & Fraternali 2011).

Resolving the structure of the H_I gas in other galaxies is observationally challenging. In recent years, the HALOGAS survey (Heald et al. 2011) has revealed the presence of an extended H_I disc around edge-on, nearby galaxies (Zschaechner et al. 2011, 2012; Gentile et al. 2013). These observations complement older detection of gaseous haloes, for example around NGC 891 by Oosterloo, Fraternali & Sancisi (2007). Most of these detections revealed a vertical lag of the H_I rotation speed above the galaxy discs of the same order of magnitude than in the Milky Way (but see also Kamphuis et al. 2013).

Given the star-forming, spiral nature of HCG 91c, it does not appear unreasonable to assume that it possesses a multiphase, complex gaseous halo similar to that of the Milky Way. Especially, although we do not know its detailed structure, the VLA observations clearly reveal a large rotating H_I reservoir. Under these circumstances, could the C1, C2 and C3 star-forming regions have resulted from

the infall and subsequent collapse of pre-existing gas clouds at the disc–halo interface of HCG 91c? The compact nature of these star-forming regions could be naturally explained by a 'localized cloud' origin. Their velocity lag of $5\text{--}10 \text{ km s}^{-1}$ would suggest that these star-forming regions are in fact not located within the disc of HCG 91c, but 300–700 pc above it, if one assumes a vertical rotational velocity lag of $15 \text{ km s}^{-1} \text{ kpc}^{-1}$ (Marasco & Fraternali 2011). Of course, the face-on nature of HCG 91c makes it impossible to directly measure any vertical offset for these star-forming regions. However, we note that the associated reddening is lower in the C1, C2 and C3 regions ($A_V \leq 0.9$, see Fig. 3) than in any other star-forming regions in the spiral arms of HCG 91c ($A_V \geq 1.2$) at the 1σ level. A lower reddening value may be the result of the location of the C1, C2 and C3 regions above the main disc (and dust) of HCG 91c.

5.2 Star formation triggering mechanism

Clearly, we cannot firmly rule out any of the above scenarios invoked to explain the origin of the anomalous star-forming regions C1, C2, and C3 in HCG 91c. At this stage, we favour the idea that these star-forming regions originated in the infall and subsequent collapse of pre-existing gas clouds at the disc–halo interface. Indeed, collapsing pre-existing gas clouds at the disc–halo interface could naturally explain the different properties of the anomalous star-forming regions (velocity lag, lower oxygen abundance, compactness).

The precise mechanism able to trigger the collapse of neutral gas clouds at the disc–halo interface of HCG 91c (and the subsequent rapid formation of molecular gas to fuel star formation) remains undefined. In the Milky Way, molecular hydrogen was detected in several IVCs (Richter et al. 2003; Wakker 2006), and it has been proposed that neutral hydrogen is compressed into molecular hydrogen as gas clouds fall on to the galaxy disc and get compressed via ram pressure stripping (Weiβ et al. 1999; Gillmon & Shull 2006; Röhser et al. 2014). The C1, C2 and C3 star-forming regions may have resulted from a boosted version of this mechanism, where the initial infall of neutral gas clouds on to the galaxy disc is being triggered by large-scale gravitational perturbations from nearby galaxies in a harassment-like process (Moore, Lake & Katz 1998). The existence of tidal perturbations to the north-west of HCG 91c (supported by the existence of a possible H_I tail and the comparatively complex edge of the stellar disc to the north-west of HCG 91c) may have given rise to local tidal shears or compressive tides (Renaud et al. 2008, 2009), triggering the collapse of the clouds. Theoretically, Renaud et al. (2014) observed the effect of compressive turbulence and how it can lead to starburst events in interacting galaxies. This mechanism is already active during the early phase of galaxy interactions, and could therefore be active in HCG 91c. In the same simulations, large-scale gas flows across a galaxy's disc only occur at later stages of the interaction (i.e. at the second closest approach). We note that the initial star formation triggered by compressive turbulence does not appear to require large velocity dispersions ($\sigma < 20 \text{ km s}^{-1}$), which would be consistent with our WiFeS observations.

Alternatively, HCG 91c is located $\sim 30 \text{ arcsec} = 15 \text{ kpc}$ (on sky) to the north-east of the extended tidal tail of HCG 91a (see Fig. 6). HCG 91c's H_I envelope also suggest that the galaxy may have previously interacted with HCG 91b (as indicated by the presence of a possible H_I bridge between the two galaxies). Ram pressure from either interaction may have shocked and compressed HCG 91c's halo, leading to the collapse of the C1, C2 and C3 star-forming regions. Kinematically, HCG 91c and the tidal tail from HCG 91a

are offset by $\sim 250 \text{ km s}^{-1}$, but given their spatial location, it is possible that HCG 91c is currently interacting/colliding with this extended tidal structure. Such a collision is impossible to firmly rule out without X-ray observations of the group which may reveal the presence of hot, shocked gas resulting from the interaction. In any case, the relatively undisturbed H α envelope of HCG 91c and the continuous structure of the tidal tail stemming from HCG 91a detected by the VLA would suggest that their interaction is at an early stage.

5.3 Constraining the exact nature of the C1, C2 and C3 regions

Our WiFeS observations, combined to VLA and Pan-STARRS data sets, have revealed the anomalous oxygen abundance of three compact star-forming regions in the disc of HCG 91c, and showed that this galaxy is only just beginning its interaction with the compact group HCG 91. From the ionized gas physical characteristics and kinematics, we found that infalling (and subsequently collapsing) gas clouds at the disc–halo interface could naturally explain the anomalous nature of the C1, C2 and C3 regions. However, one should keep in mind that our different pieces of evidence for the anomalous nature of the C1, C2 and C3 star-forming regions (velocity and abundance offset, lower extinction) are all at the 1σ – 2σ level.

We also lack critical pieces of information: for example, a deeper understanding of the state of the gas (i.e. pressure, density, temperature) in these specific star-forming regions, as well as a better characterization of the underlying stellar population. Additional insight on the stellar population associated with the C1, C2 and C3 regions is especially critical to test their possible origins. For example, collapsing halo gas clouds with masses ranging from 10^3 – $10^5 M_\odot$ (see Putman et al. 2012, and references therein) do not offer a sustainable source of fuel and cannot host a significant population of old stars, of which the detection would be a very strong argument *against* this scenario. Unfortunately, the S/N in the continuum of our observations does not allow us to extract meaningful information on the underlying stellar population in HCG 91c (see Fig. 18).

The inherent compact aspect of the C1, C2 and C3 regions would also benefit from a finer spatial sampling to reveal their precise structural extent and possible physical connections. Finally, the disc of HCG 91c extends beyond the field of view of our WiFeS observations, and may contain additional anomalous star-forming regions. To address these questions, we have been awarded 4.0 h of Science Verification time on MUSE (Bacon et al. 2010), the new integral field spectrograph on the Yepun telescope (unit 4 of the VLT) at Paranal in Chile (P.I. F. P. A. Vogt, P.Id. 60.A-9317[A]), which will be the subject of a separate paper.

We have shown that overall, HCG 91c is a largely undisturbed (yet) star-forming spiral galaxy. Hence, HCG 91c offers us a window on the early stage of galaxy interactions in a compact group, and possibly on the early phase of galaxy pre-processing in these environments. The presence of localized star-forming regions with lower oxygen abundances indicate that lower metallicity gas is being brought from the outer regions of the disc or the halo to the inner regions of the galaxy. Hence, this gas may eventually contribute to the flattening of the oxygen abundance gradient in the system. Strong interactions of galaxies in pairs have been observed to flatten the metallicity gradient in these systems through large-scale gas flows (Kewley et al. 2010; Rupke, Kewley & Chien 2010). Our WiFeS observations of HCG 91c suggest that prior to large-scale gas flows induced by strong gravitational perturbation, some gas

mixing can be occurring at the level of individual star-forming regions as a result of galaxy harassment and longer range gravitational interactions.

Evaluating the ubiquity (or not) of collapsing gas clouds at the disc–halo interface of galaxies as an early consequence of galaxy harassment will require additional observations of a statistical sample of galaxies. Existing or upcoming IFS surveys such as SAMI or MaNGA may provide such a statistical sample probing a wide range of environment densities. However, with a respective spectral resolution of $R = 4500$ and 2000 and a spatial sampling $\geq 1 \text{ kpc}$, finding sub-kpc star-forming regions with ~ 0.15 dex oxygen abundances offsets will certainly prove challenging for these surveys. Rather than ‘direct’ detections, the SAMI and MaNGA surveys may instead provide ‘tentative’ detections of anomalous star-forming regions in largely unperturbed star-forming disc galaxies. These objects would form an ideal sample (spanning a wide range of environments) for dedicated follow-up observations at higher spectral and spatial resolution. In fact, we expect that large IFS surveys will provide an essential data base allowing the identification of largely undisturbed galaxies (similar to HCG 91c) in the early stage of their interaction with a compact group or cluster. As yet mostly unaffected by their environments, these systems can shine a unique light on the early stages of complex gravitational interactions and the associated consequences.

6 SUMMARY

In this paper, we presented the discovery of three compact star-forming regions with oxygen abundance and kinematic anomalies (at the 1σ – 2σ level) in the otherwise unremarkable star-forming spiral galaxy HCG 91c. From the analysis of the different strong optical emission lines detected with WiFeS, we found these anomalous star-forming regions (a) to be comparatively more metal-poor by 0.15 dex with respect to their surroundings, and as expected from the overall metallicity gradient present in the inner region of HCG 91c, (b) to kinematically lag behind the disc rotation by 5 – 10 km s^{-1} , and (c) for one of them, to be associated with the highest value of the ionization parameter in the entire galaxy ($\log(q) \approx 7.95$).

To understand the origin of these peculiar star-forming regions, we combined our WiFeS data set with broad-band images of HCG 91c from Pan-STARRS, and with VLA observations of the group-wide H α distribution of HCG 91. These data sets reveal that HCG 91c is still largely undisturbed, but most likely experiencing the very first stage of its gravitational interactions with other galaxies inside HCG 91 (and possibly with the large tidal tail from HCG 91a).

Under these circumstances, we discussed three possible scenarios to explain the origin of the anomalous star-forming regions detected with WiFeS: accretion of a satellite, gas inflow from the halo and collapsing pre-existing gas clouds at the disc–halo interface. We found that the latter scenario could naturally explain all of the observed characteristics of the anomalous star-forming regions (lower metallicity, velocity lag, compactness, lower reddening). By comparison, the satellite accretion and gas inflows scenarios are harder to reconcile with the observed gas kinematics, but cannot be firmly ruled out at this stage.

We discussed possible mechanisms able to trigger star formation in these originally stable, pre-existing gas clouds, in the form of tidal shears, long-range gravitational perturbations or harassment from the other group members. Theoretically, these scenarios are consistent with the recent simulations of Renaud et al. (2014) suggesting that compressive turbulence is responsible for enhanced star

formation activity in the very early stages of galaxy interactions, while large-scale gas flows within a galaxy disc feeding central starbursts occur later on at the second closest approach.

HCG 91c may be offering a direct window on the early phase of galaxy interactions in compact group environments, and possibly on one of the early stage of galaxy evolution. The existence of localized regions of lower metallicity gas suggest that gas mixing (leading to a flattening of the overall abundance gradient) can be occurring on the scales of individual star-forming regions before the onset of large inflows following stronger gravitational effects. In the era of large-scale IFS surveys such as CALIFA, SAMI and MaNGA, HCG 91c act as a reminder that mechanisms associated with galaxy evolution may first be impactful on sub-kpc scale and display a discreet kinematic signature ($\Delta v \approx 10 \text{ km s}^{-1}$ in the present case).

Dedicated follow-up MUSE observations will provide us with a sharper view of HCG 91c and its peculiar star-forming regions. This data set ought to let us better characterize the physical conditions of the ionized gas throughout HCG 91c, refine our detections of lower abundances, kinematic offsets and reduced extragalactic reddening associated with the C1, C2 and C3 star-forming regions, as well as provide important information regarding their underlying stellar population. The MUSE observations will be key to test our current favoured scenario for explaining the lower oxygen abundances of the C1, C2 and C3 regions, and let us identify whether additional star-forming regions in the outer regions of HCG 91c (undetected with WiFeS) display similar gaseous abundance anomalies.

ACKNOWLEDGEMENTS

We thank I-Ting Ho for sharing his LZIFU IDL routine with us, Bill Roberts and the IT team at the Research School of Astronomy and Astrophysics (RSAA) at the Australian National University (ANU) for their support installing and maintaining the PDF3DREPORTGEN software on the school servers, and the anonymous referee for his/her constructive suggestions. FPAV acknowledges a Fulbright scholarship, and further financial support from the Alex Rodgers Travelling scholarship from the RSAA at the ANU. He is also grateful to the Department of Physics and Astronomy at Johns Hopkins University for hosting him during his Fulbright exchange. MAD acknowledges the support of the Australian Research Council (ARC) through Discovery project DP130103925, and additional financial support for this project from King Abdulaziz University. This research has made use of the ALADIN interactive sky atlas (Bonnarel et al. 2000), and of NASA's Astrophysics Data System and the NED which is operated by the Jet Propulsion Laboratory, California Institute of Technology, under contract with the National Aeronautics and Space Administration. This research also made use of STATSMODEL (Seabold & Perktold 2010), of MATPLOTLIB (Hunter 2007), of ASTROPY, a community-developed core PYTHON package for Astronomy (Astropy Collaboration et al. 2013), of MAYAVI (Ramachandran & Varoquaux 2011), of APLPY, an open-source plotting package for PYTHON hosted at <http://aplpy.github.com>, and of MONTAGE, funded by the National Aeronautics and Space Administration's Earth Science Technology Office, Computation Technologies Project, under Cooperative Agreement Number NCC5-626 between NASA and the California Institute of Technology. MONTAGE is maintained by the NASA/IPAC Infrared Science Archive. The 'Second Epoch Survey' of the southern sky was made by the Anglo-Australian Observatory (AAO) with the UK Schmidt Telescope. Plates from this survey have been digitized and compressed at the Space Telescope Science Institute under US Government grant NAG W-2166. The Pan-STARRS1 Surveys (PS1) have been made possible through contributions of the

Institute for Astronomy, the University of Hawaii, the Pan-STARRS Project Office, the Max-Planck Society and its participating institutes, the Max Planck Institute for Astronomy, Heidelberg and the Max Planck Institute for Extraterrestrial Physics, Garching, The Johns Hopkins University, Durham University, the University of Edinburgh, Queen's University Belfast, the Harvard-Smithsonian Center for Astrophysics, the Las Cumbres Observatory Global Telescope Network Incorporated, the National Central University of Taiwan, the Space Telescope Science Institute, the National Aeronautics and Space Administration under Grant No. NNX08AR22G issued through the Planetary Science Division of the NASA Science Mission Directorate, the National Science Foundation under Grant No. AST-1238877, the University of Maryland, and Eotvos Lorand University (ELTE). We thank the PS1 Builders and PS1 operations staff for construction and operation of the PS1 system and access to the data products provided.

REFERENCES

- Allen M. G., Groves B. A., Dopita M. A., Sutherland R. S., Kewley L. J., 2008, *ApJS*, 178, 20
 Amram P., Plana H., Mendes de Oliveira C., Balkowski C., Boulesteix J., 2003, *A&A*, 402, 865
 Appleton P. N. et al., 2006, *ApJ*, 639, L51
 Astropy Collaboration et al., 2013, *A&A*, 558, A33
 Bacon R. et al., 2001, *MNRAS*, 326, 23
 Bacon R. et al., 2010, in McLean I. S., Ramsay S. K., Takami H., eds, Proc. SPIE Conf. Ser. Vol. 7735, Ground-based and Airborne Instrumentation for Astronomy III. SPIE, Bellingham, p. 773508
 Barnes D. G., Fluke C. J., 2008, *New Astron.*, 13, 599
 Barnes D. G., Webster R. L., 2001, *MNRAS*, 324, 859
 Belokurov V. et al., 2006, *ApJ*, 642, L137
 Binette L., Dopita M. A., Dodorico S., Benvenuti P., 1982, *A&A*, 115, 315
 Binette L., Dopita M. A., Tuohy I. R., 1985, *ApJ*, 297, 476
 Bitsakis T., Charmandaris V., Appleton P. N., Diaz-Santos T., Le Floc'h E., da Cunha E., Alatalo K., Cluver M., 2014, *A&A*, 565, A25
 Blanc G. A. et al., 2013, *AJ*, 145, 138
 Blanc G. A., Kewley L., Vogt F. P. A., Dopita M. A., 2015, *ApJ*, 798, 99
 Bonnarel F. et al., 2000, *A&AS*, 143, 33
 Borthakur S., Yun M. S., Verdes-Montenegro L., 2010, *ApJ*, 710, 385
 Bundy K. et al., 2014, *ApJ*, 798, 7
 Calzetti D., Armus L., Bohlin R. C., Kinney A. L., Koornneef J., Storchi-Bergmann T., 2000, *ApJ*, 533, 682
 Calzetti D. et al., 2007, *ApJ*, 666, 870
 Cappellari M., Emsellem E., 2004, *PASP*, 116, 138
 Cappellari M. et al., 2007, *MNRAS*, 379, 418
 Cappellari M. et al., 2011, *MNRAS*, 413, 813
 Childress M., Vogt F., Nielsen J., Sharp R., 2014a, *Astrophysics Source Code Library*, record ascl:1402.034
 Childress M. J., Vogt F. P. A., Nielsen J., Sharp R. G., 2014b, *Ap&SS*, 349, 617
 Cluver M. E. et al., 2010, *ApJ*, 710, 248
 Cluver M. E. et al., 2013, *ApJ*, 765, 93
 Cortese L., Gavazzi G., Boselli A., Franzetti P., Kennicutt R. C., O'Neil K., Sakai S., 2006, *A&A*, 453, 847
 Coziol R., Plauchu-Frayn I., 2007, *AJ*, 133, 2630
 Croom S. M. et al., 2012, *MNRAS*, 421, 872
 Cybulski R., Yun M. S., Fazio G. G., Gutermuth R. A., 2014, *MNRAS*, 439, 3564
 de la Rosa I. G., de Carvalho R. R., Vazdekis A., Barbry B., 2007, *AJ*, 133, 330
 de Vaucouleurs G., de Vaucouleurs A., Corwin H. G., Jr Buta R. J., Paturel G., Fouqué P., 1991, *Third Reference Catalogue of Bright Galaxies*. Volume I: Explanations and references. Volume II: Data for galaxies between 0^h and 12^h . Volume III: Data for galaxies between 12^h and 24^h . Springer-Verlag, Berlin

- de Zeeuw P. T. et al., 2002, MNRAS, 329, 513
 Desjardins T. D. et al., 2013, ApJ, 763, 121
 Desjardins T. D. et al., 2014, ApJ, 790, 132
 Dopita M. A., Binette L., Schwartz R. D., 1982, ApJ, 261, 183
 Dopita M. A. et al., 2006, ApJS, 167, 177
 Dopita M., Hart J., McGregor P., Oates P., Bloxham G., Jones D., 2007, Ap&SS, 310, 255
 Dopita M. et al., 2010, Ap&SS, 327, 245
 Dopita M. A., Sutherland R. S., Nicholls D. C., Kewley L. J., Vogt F. P. A., 2013, ApJS, 208, 10
 Dopita M. A., Rich J., Vogt F. P. A., Kewley L. J., Ho I.-T., Basurah H. M., Ali A., Amer M. A., 2014, Ap&SS, 350, 741
 Dopita M. A. et al., 2014, A&A, 566, A41
 Dopita M. A. et al., 2015, ApJS, 217, 12
 Driver S. P. et al., 2009, Astron. Geophys., 50, 5.12
 Drory N. et al., 2015, AJ, 149, 77
 Emsellem E. et al., 2004, MNRAS, 352, 721
 Fischer J., Dopita M., 2005, ApJ, 619, 340
 Fitzpatrick E. L., 1999, PASP, 111, 63
 Gallagher S. C., Johnson K. E., Hornschemeier A. E., Charlton J. C., Hibbard J. E., 2008, ApJ, 673, 730
 Gentile G. et al., 2013, A&A, 554, A125
 Gillmon K., Shull J. M., 2006, ApJ, 636, 908
 González Delgado R. M., Cerviño M., Martins L. P., Leitherer C., Hauschildt P. H., 2005, MNRAS, 357, 945
 Groves B. A., Dopita M. A., Sutherland R. S., 2004, ApJS, 153, 9
 Heald G. et al., 2011, A&A, 526, A118
 Hickson P., 1982a, ApJ, 255, 382
 Hickson P., 1982b, ApJ, 259, 930
 Hickson P., Mendes de Oliveira C., Huchra J. P., Palumbo G. G., 1992, ApJ, 399, 353
 Ho I.-T. et al., 2014, MNRAS, 444, 3894
 Hodapp K. W. et al., 2004, Astron. Nachr., 325, 636
 Hunter J. D., 2007, Comput. Sci. Eng., 9, 90
 Iovino A., 2002, AJ, 124, 2471
 Johnson K. E., Hibbard J. E., Gallagher S. C., Charlton J. C., Hornschemeier A. E., Jarrett T. H., Reines A. E., 2007, AJ, 134, 1522
 Jones D. H. et al., 2004, MNRAS, 355, 747
 Jones D. H. et al., 2009, MNRAS, 399, 683
 Kaiser N., 2004, in Oschmann J. M., Jr, ed., Proc. SPIE Conf. Ser. Vol. 5489, Ground-based Telescopes. SPIE, Bellingham, p. 11
 Kaiser N. et al., 2002, in Tyson J. A., Wolff S., eds, Proc. SPIE Conf. Ser. Vol. 4836, Survey and Other Telescope Technologies and Discoveries. SPIE, Bellingham, p. 154
 Kaiser N. et al., 2010, in Stepp L. M., Gilmozzi R., Hall H. J., eds, Proc. SPIE Conf. Ser. Vol. 7733, Ground-based and Airborne Telescopes III. SPIE, Bellingham, p. 77330E
 Kalberla P. M. W., Kerp J., 2009, ARA&A, 47, 27
 Kamphuis P. et al., 2013, MNRAS, 434, 2069
 Kauffmann G. et al., 2003, MNRAS, 346, 1055
 Kennicutt R. C., Jr, 1998, ApJ, 498, 541
 Kennicutt R. C., Evans N. J., 2012, ARA&A, 50, 531
 Kent B. R., 2013, PASP, 125, 731
 Kewley L. J., Heisler C. A., Dopita M. A., Lumsden S., 2001, ApJS, 132, 37
 Kewley L. J., Groves B., Kauffmann G., Heckman T., 2006, MNRAS, 372, 961
 Kewley L. J., Rupke D., Zahid H. J., Geller M. J., Barton E. J., 2010, ApJ, 721, L48
 Komatsu E. et al., 2011, ApJS, 192, 18
 Krajanović D., Cappellari M., de Zeeuw P. T., Copin Y., 2006, MNRAS, 366, 787
 Krajanović D. et al., 2011, MNRAS, 414, 2923
 Kroupa P., 2001, MNRAS, 322, 231
 Lara-López M. A. et al., 2013, MNRAS, 434, 451
 Lauberts A., Valentijn E. A., 1989, The Surface Photometry Catalogue of the ESO-Uppsala Galaxies. ESO, Garching
 Leitherer C. et al., 1999, ApJS, 123, 3
- Magnier E., 2007, in Sterken C., ed., ASP Conf. Ser. Vol. 364, The Future of Photometric, Spectrophotometric and Polarimetric Standardization. Astron. Soc. Pac., San Francisco, p. 153
 Magnier E. A. et al., 2013, ApJS, 205, 20
 Marasco A., Fraternali F., 2011, A&A, 525, A134
 Markwardt C. B., 2009, in Bohlander D. A., Durand D., Dowler P., eds, ASP Conf. Ser. Vol. 411, Astronomical Data Analysis Software and Systems XVIII. Astron. Soc. Pac., San Francisco, p. 251
 Mathewson D. S., Hart J., Wehner H. P., Hovey G. R., van Harmelen J., 2013, J. Astron. Hist. Heritage, 16, 2
 Mendes de Oliveira C., Amram P., Plana H., Balkowski C., 2003, AJ, 126, 2635
 Moore B., Lake G., Katz N., 1998, ApJ, 495, 139
 Murphy E. J. et al., 2011, ApJ, 737, 67
 Nicholls D. C., Dopita M. A., Sutherland R. S., 2012, ApJ, 752, 148
 Nicholls D. C., Dopita M. A., Sutherland R. S., Kewley L. J., Palay E., 2013, ApJS, 207, 21
 Oosterloo T., Fraternali F., Sancisi R., 2007, AJ, 134, 1019
 Osterbrock D. E., 1989, Astrophysics of Gaseous Nebulae and Active Galactic Nuclei. University Science Books, Mill Valley, CA
 Plauchu-Frayn I., Del Olmo A., Coziol R., Torres-Papaqui J. P., 2012, A&A, 546, A48
 Ponman T. J., Bourner P. D. J., Ebeling H., Böhringer H., 1996, MNRAS, 283, 690
 Putman M. E., Peek J. E. G., Joung M. R., 2012, ARA&A, 50, 491
 Ramachandran P., Varoquaux G., 2011, Comput. Sci. Eng., 13, 40
 Rasmussen J., Ponman T. J., Verdes-Montenegro L., Yun M. S., Borthakur S., 2008, MNRAS, 388, 1245
 Rasmussen J., Mulchaey J. S., Bai L., Ponman T. J., Raychaudhury S., Dariush A., 2012, ApJ, 757, 122
 Renaud F., Boily C. M., Fleck J.-J., Naab T., Theis C., 2008, MNRAS, 391, L98
 Renaud F., Boily C. M., Naab T., Theis C., 2009, ApJ, 706, 67
 Renaud F., Bournaud F., Kraljic K., Duc P.-A., 2014, MNRAS, 442, L33
 Rich J. A., Dopita M. A., Kewley L. J., Rupke D. S. N., 2010, ApJ, 721, 505
 Richardson J. C. et al., 2011, ApJ, 732, 76
 Richter P., Wakker B. P., Savage B. D., Sembach K. R., 2003, ApJ, 586, 230
 Röhser T., Kerp J., Winkel B., Boulanger F., Lagache G., 2014, A&A, 564, A71
 Rosales-Ortega F. F., Kennicutt R. C., Sánchez S. F., Díaz A. I., Pasquali A., Johnson B. D., Hao C. N., 2010, MNRAS, 405, 735
 Rubin V. C., Hunter D. A., Ford W. K., Jr, 1991, ApJS, 76, 153
 Rupke D. S. N., Kewley L. J., Chien L.-H., 2010, ApJ, 723, 1255
 Sánchez S. F. et al., 2012, A&A, 538, A8
 Saul D. R. et al., 2012, ApJ, 758, 44
 Schlafly E. F., Finkbeiner D. P., 2011, ApJ, 737, 103
 Schlegel D. J., Finkbeiner D. P., Davis M., 1998, ApJ, 500, 525
 Seabold J. S., Perktold J., 2010, in van der Walt S., Millman J. eds, Proc. 9th Python in Science Conf., p. 57, available at: <http://conference.scipy.org/proceedings/scipy2010/pdfs/proceedings.pdf>
 Skrutskie M. F. et al., 2006, AJ, 131, 1163
 Sutherland R. S., Dopita M. A., 1993, ApJS, 88, 253
 Tonry J. L. et al., 2012, ApJ, 750, 99
 Torres-Flores S., Mendes de Oliveira C., Amram P., Plana H., Epinat B., Carignan C., Balkowski C., 2010, A&A, 521, A59
 Torres-Flores S., Mendes de Oliveira C., Plana H., Amram P., Epinat B., 2013, MNRAS, 432, 3085
 Tzanavaris P. et al., 2010, ApJ, 716, 556
 Verdes-Montenegro L., Yun M. S., Williams B. A., Huchtmeier W. K., Del Olmo A., Perea J., 2001, A&A, 377, 812
 Vijayaraghavan R., Ricker P. M., 2013, MNRAS, 435, 2713
 Vogt F. P. A., Dopita M. A., Kewley L. J., 2013, ApJ, 768, 151
 Wakker B. P., 2001, ApJS, 136, 463
 Wakker B. P., 2006, ApJS, 163, 282
 Wakker B. P., van Woerden H., 1997, ARA&A, 35, 217
 Walker L. M., Johnson K. E., Gallagher S. C., Hibbard J. E., Hornschemeier A. E., Tzanavaris P., Charlton J. C., Jarrett T. H., 2010, AJ, 140, 1254

- Walker L. M., Johnson K. E., Gallagher S. C., Charlton J. C., Hornschemeier A. E., Hibbard J. E., 2012, AJ, 143, 69
 Weiß A., Heithausen A., Herbstmeier U., Mebold U., 1999, A&A, 344, 955
 Westmoquette M. S., Exter K. M., Smith L. J., Gallagher J. S., 2007, MNRAS, 381, 894
 Wijesinghe D. B. et al., 2011, MNRAS, 410, 2291
 Zschaechner L. K., Rand R. J., Heald G. H., Gentile G., Kamphuis P., 2011, ApJ, 740, 35
 Zschaechner L. K., Rand R. J., Heald G. H., Gentile G., Józsa G., 2012, ApJ, 760, 37

APPENDIX A: COMPARISON OF THE GAS KINEMATICS WITH AMRAM ET AL. (2003)

Amram et al. (2003) presented Fabry–Perot observations of the H α emission line in the galaxy HCG 91c, and reported the existence of large asymmetries and multiple distinct components in the line profile (see their fig. 20). Their data was acquired with the CIGALE Fabry–Perot mounted on the *ESO 3.6 m telescope* at La Silla on 1995 August 21–24 with a seeing of ~ 1 arcsec. The spectral resolution of their data set was $R = 9375$ at H α , with 24 scanning steps and a sampling step of 0.35 Å or ~ 16 km s $^{-1}$, and a spatial pixel size of 0.91×0.91 arcsec 2 .

In Fig. A1, we reproduce the fig. 20 of Amram et al. (2003) showing the H α line profile for the central 15×15 arcsec 2 regions of HCG 91c, but for our WiFeS data. Modulo minor differences (i.e. each panel corresponds to 1×1 arcsec 2 instead of 0.91×0.91 arcsec 2), both figures are directly comparable. Especially, each panel in our Fig. A1 covers the same spectral range as fig. 20 of Amram et al. (2003).

These authors reports secondary velocity components redshifted by ~ 100 km s $^{-1}$ from the main line peak, and with dispersion extending over the entire spectral range shown in the different panels. It is clear from Fig. A1 that despite the slightly lower spectral resolution ($R = 7000$) and spectral sampling (0.44 Å or ~ 19.5 km s $^{-1}$) of our data set, WiFeS would have detected complex line profiles

such as those reported by Amram et al. (2003). Instead, the H α line profiles observed by WiFeS are narrow (with $\sigma \approx 20\text{--}40$ km s $^{-1}$, see Section 4.4) and single-peaked. We detect some small asymmetries in the inner most spaxels consistent with beam smearing. We note that these asymmetries are mostly *blueshifted* with respect to the main line peak, while the asymmetries reported by Amram et al. (2003) are largely *redshifted*.

As we find no evidence for multiple kinematics components in our WiFeS observations of HCG 91c – and especially find no evidence for the complex line profiles reported by Amram et al. (2003) – we are lead to conclude that the gas in this galaxy can be well described by a single kinematic structure at all locations.

APPENDIX B: ERROR PROPAGATION IN PYQZ v0.6.0

In the original version published by Dopita et al. (2013), the PYQZ v0.4.0 module was not set up to account for errors in the flux measurements of emission lines. Instead, errors on the estimation of $\log(q)$ and $12 + \log(\text{O/H})$ were estimated from the standard deviation between the different estimates stemming from the different line ratio diagnostic grids chosen by the user. Indeed, for flux measurements at the ~ 5 per cent level, the mismatch between the estimates from different diagnostics typically dominates the uncertainty of the joint final estimate. For larger observational errors on the emission line fluxes, PYQZ v0.4.0 therefore underestimates the true error associated with the final values of $12 + \log(\text{O/H})$ and $\log(q)$. Here, we have upgraded PYQZ to address this shortcoming. The updated version of PYQZ will be publicly released and described in details in the near future along with new MAPPINGS IV models. Here, we briefly describe for completeness how errors on the final $12 + \log(\text{O/H})$ and $\log(q)$ estimates in our analysis of HCG 91c are computed.

The underlying idea is to propagate the full probability density function associated with each line flux measurement to the $12 + \log(\text{O/H})$ versus $\log(q)$ plane. To that end, for each set of line

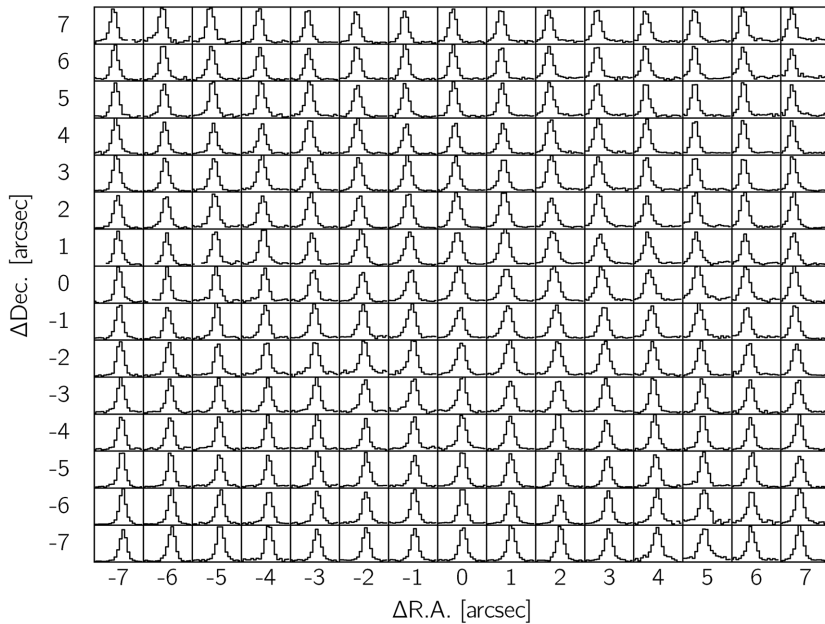


Figure A1. Reproduction of fig. 20 of Amram et al. (2003), but for our WiFeS observations: the H α line profile for all the spaxels within a box of 15×15 arcsec 2 centred on the galaxy’s core (i.e. spaxel [0;0] in our reference frame). Each panel contains 19 wavelengths bins ranging from 6719.56 to 6727.48 Å. Each panel is normalized to the emission line peak.

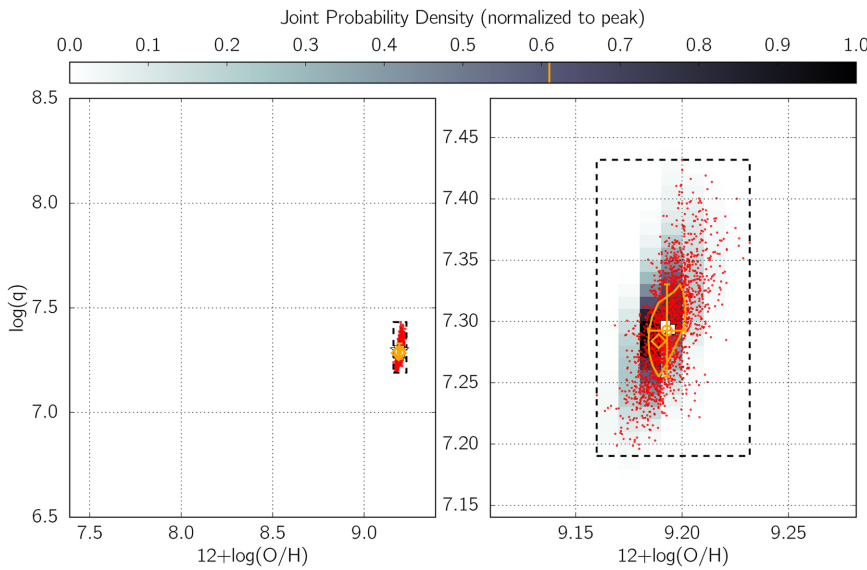


Figure B1. Full (left) and magnified (right) oxygen abundance and ionization parameter plane accessible to PYQZ v0.6.0. The data corresponds to the spaxel [0;0] in our observations of HCG 91c. The white squares mark the two estimates associated with the diagnostic grids $\log [\text{N II}]/[\text{S II}]$ versus $\log [\text{O III}]/\text{H}\beta$ and $\log [\text{N II}]/[\text{S II}]$ versus $\log [\text{O III}]/[\text{S II}]$. The red dots mark the location of 2×1000 randomly-reconstructed line fluxes from the original line fluxes and associated errors. The reconstructed 2D joint probability density distribution [with a fixed resolution of 0.01 in $12+\log (\text{O/H})$ and 0.01 in $\log (q)$] is also shown, with the orange contour tracing the 1σ level from the peak. The peak location is marked with an orange diamond, while the mean location of the 1σ contour and its extent in marked with the orange circle and associated error bars. The dashed box marks the full extent of the random set of individual estimates (the red dots).

fluxes (and errors) provided by the user (i.e. for each individual spaxel, in the case of our analysis), PYQZ v0.6.0 generates n random set of line fluxes from the errors provided by the user, assuming a normal and uncorrelated error distribution for each line. PYQZ subsequently derives an estimate of $12+\log (\text{O/H})$ and $\log (q)$ for all n set of random line fluxes, and for every line ratio diagnostic grid selected by the user, resulting in $n \times m$ estimates of $12+\log (\text{O/H})$ and $\log (q)$ (where m is the number of line ratio grids selected by the user). Effectively, these $n \times m$ estimates represent the discretized two-dimensional joint probability distribution function of the oxygen abundance and ionization parameter. The full joint probability density function can then be reconstructed by performing a two-dimensional kernel density estimation. This frequentist approach to error estimation differs from the Bayes formalism adopted by Blanc et al. (2015) in the IZI code written in IDL with a similar purpose to PYQZ.

It is often practical to derive from the joint probability density function a *best estimate* and associated uncertainty. To derive the best estimate for $12+\log (\text{O/H})$ and $\log (q)$, PYQZ normalizes the reconstructed joint probability function to its peak level, and computes the 61 per cent-level contour (corresponding the 1σ level for a normal distribution). The mean location of this contour is then chosen as the best estimate of the $12+\log (\text{O/H})$ and $\log (q)$, while the full extent of the contour is indicative of the uncertainty associated with these estimates.

The process is illustrated for two representative high and low S/N spaxels in our WiFeS observations of HCG 91c in Figs B1 and B2, respectively. For reasons detailed in Section 4.3, these examples rely on only two line ratio diagnostic grids: $\log [\text{N II}]/[\text{S II}]$ versus $\log [\text{O III}]/\text{H}\beta$ and $\log [\text{N II}]/[\text{S II}]$ versus $\log [\text{O III}]/[\text{S II}]$. The location of the individual estimates stemming from either diagnostic grids in the $12+\log (\text{O/H})$ versus $\log (q)$ are marked with white squares. The mean of these positions, corresponding to the PYQZ v0.4.0 estimate of $12+\log (\text{O/H})$ and $\log (q)$, is marked with a white star. For both spaxels, 1000 random set of line fluxes were

generated by PYQZ, resulting in 2000 estimates of $12+\log (\text{O/H})$ and $\log (q)$ (1000 for either line ratio grid), shown as individual red dots.

The 61 per cent-of-peak-level contour of the underlying reconstructed joint probability density function is shown with an orange line. With 1000 random sets of line fluxes, we find that the location of the peak of the joint probability density function (marked with an orange diamond symbol) varies within the 1σ contours when PYQZ is run multiple times. However, the location of the 1σ contour at 61 per cent of the peak level remains consistent when PYQZ is run multiple times. This fact motivates our choice to base the final estimates of $12+\log (\text{O/H})$ and $\log (q)$ on the mean location of the 1σ contour level, rather than the exact peak location.

Different PYTHON tools exists to perform a two-dimensional kernel density estimation. PYQZ can be set by the user to use two of these – either the GAUSSIAN_KDE routine in the SCIPY.STATS package,⁸ or the KDEMULTIVARIATE routine in the STATSMODEL package.⁹ The former routine is 10–100 times faster but is not well suited for bi- or multimodal distributions. In the case of PYQZ, the GAUSSIAN_KDE routine tends to oversmooth the joint probability function when two diagnostics are not directly consistent with one another (for example in the case of a flux measurement error). The option to use the GAUSSIAN_KDE routine is included in PYQZ v0.6.0 as a rapid alternative to test the code and obtain preliminary results. In practice, it is preferable to use the KDEMULTIVARIATE routine instead which provides more accurate results, as the bandwidth of the Gaussian kernel can be set individually for the $12+\log (\text{O/H})$ and $\log (q)$ directions. All

⁸ http://docs.scipy.org/doc/scipy-0.14.0/reference/generated/scipy.stats.gaussian_kde.html, accessed on 2014 December 13.

⁹ http://statsmodels.sourceforge.net/devel/generated/statsmodels.nonparametric.kernel_density.KDEMultivariate.html, accessed on 2014 December 13.

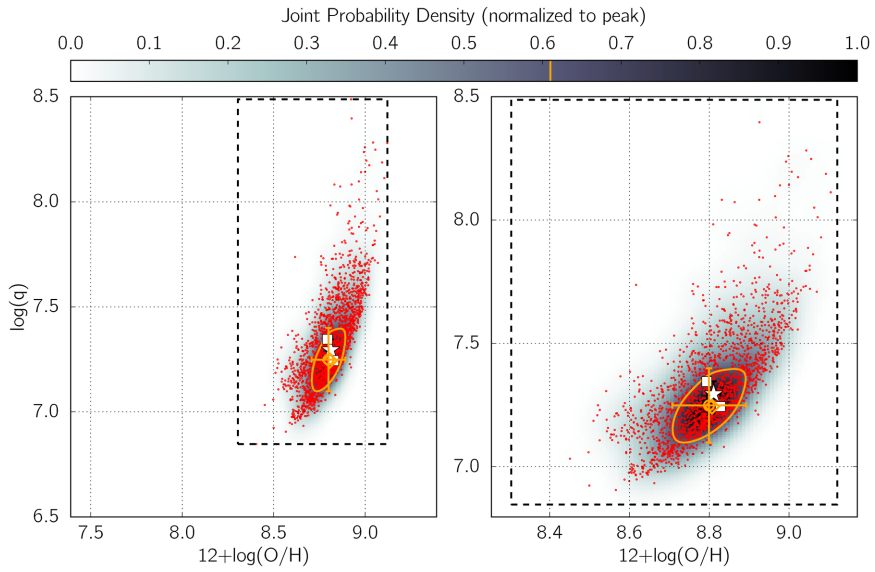


Figure B2. Same as Fig. B1, but for the spaxel [9;14]. The lower S/N in the data results in a larger spread of the random set of estimates.

estimates of oxygen abundances and ionization parameters presented in this paper were derived using the `KDEMULTIVARIATE` method.

SUPPORTING INFORMATION

Additional Supporting Information may be found in the online version of this article:

HCG91_HI_3d.html (<http://mnras.oxfordjournals.org/lookup/suppl/doi:10.1093/mnras/stv749/-DC1>).

Please note: Oxford University Press is not responsible for the content or functionality of any supporting materials supplied by the authors. Any queries (other than missing material) should be directed to the corresponding author for the article.

This paper has been typeset from a TeX/LaTeX file prepared by the author.